PLANETARY SCIENCE

History of the solar nebula from meteorite paleomagnetism

Benjamin P. Weiss[1]*, Xue-Ning Bai[2]*, Roger R. Fu[3]

We review recent advances in our understanding of magnetism in the solar nebula and protoplanetary disks (PPDs). We discuss the implications of theory, meteorite measurements, and astronomical observations for planetary formation and nebular evolution. Paleomagnetic measurements indicate the presence of fields of 0.54 ± 0.21 G at ~1 to 3 astronomical units (AU) from the Sun and ≳0.06 G at 3 to 7 AU until >1.22 and >2.51 million years (Ma) after solar system formation, respectively. These intensities are consistent with those predicted to enable typical astronomically observed protostellar accretion rates of ~10^{-8} $M_{\odot}$year^{-1}, suggesting that magnetism played a central role in mass transport in PPDs. Paleomagnetic studies also indicate fields <0.006 G and <0.003 G in the inner and outer solar system by 3.94 and 4.89 Ma, respectively, consistent with the nebular gas having dispersed by this time. This is similar to the observed lifetimes of extrasolar protoplanetary disks.

INTRODUCTION

Newly formed Sun-like stars are surrounded by planar distributions of circumstellar material known as protoplanetary disks (PPDs) (*1*). PPDs form as consequence of the collapse of molecular cloud cores under angular momentum conservation and are a critical intermediate stage of solar system formation (*2*). They consist mostly of hydrogen and helium gas, with about ~1% by mass solids (i.e., dust) that serve as the building blocks for planetary bodies. The hundreds of PPDs currently accessible to astronomical observations have typical radii of 10^1 to 10^2 astronomical units (AU) and masses ranging from 10^{-4} to 10^{-1} (median, ~10^{-2}) solar masses ($M_{\odot}$) (*2*). About half of all PPDs disperse between ~2 and 4 million years (Ma) after collapse of their parent molecular clouds (*3*, *4*). Recently, PPDs have been found to have rich substructures (*5*, *6*), which may suggest that they form planets extremely efficiently.

PPDs actively accrete onto their host protostars. Typical accretion rates are ~10^{-8} $M_{\odot}$year^{-1} for the bulk of PPD lifetimes (*7*) but can be several orders of magnitude higher at early phases and drop to <10^{-10} $M_{\odot}$ year^{-1} as disks disperse (*8*). Accretion requires efficient transport of disk angular momentum, and we will shortly show that a prominent role for magnetic fields in this process is likely unavoidable. Depending on the mechanisms involved, the expected field strength can be directly estimated for any given accretion rate. Because angular momentum transport further governs the overall gas dynamics (e.g., flow properties such as the level of turbulence) and the long-term mass evolution of the disk, it is the central focus of the theory of PPDs.

Measuring the magnetic field strength in PPDs therefore offers a unique opportunity to test disk theory with far-reaching implications for planet formation. Thus far, astronomical observations have yet to unambiguously constrain the strength and morphology of magnetic fields in the planet-forming regions of PPDs (*9*). However, beginning with the formation of calcium aluminum-rich inclusions (CAIs) at ~4567 Ma ago and lasting several Ma, our own solar system is thought to have transitioned through a PPD phase known as the solar nebula. The present-day solar system preserves a diversity of records of its formation and evolution dating back to this early epoch, largely in the form of meteorites. Recently, laboratory analyses of natural remanent magnetization (NRM) in meteorites have provided time-resolved and spatially-resolved constraints on the magnetic field intensity in the solar nebula (*10*). Because many meteoritic materials are thought to have been magnetized in the solar nebula or shortly after the solar nebula dispersed, they currently provide the best available data on magnetic fields for testing the disk theory and its relationship with solar system formation.

Here, we review recent advances in the theory of disk magnetic fields and the status and implications of astronomical and meteorite records for PPD magnetism. We discuss how meteorite studies have enabled measurements of field strength (paleointensity) over space and time and how these measurements can help distinguish between various proposed mechanisms for angular momentum transport, formation of chondrules, and the lifetime of the nebula and its implications for giant planet formation.

THEORY

Mechanisms governing angular momentum transport

Formation of PPDs from the collapse of prestellar and protostellar cores in molecular clouds is a natural consequence of angular momentum conservation. The subsequent evolution of such a disk into the present-day solar system, in which >99% of the mass is within the Sun and >99% of the angular momentum is carried by the planets, required the inward transfer of mass. Angular momentum conservation, in turn, required that the angular momentum originally carried by this mass be transferred to a smaller amount of mass that flows outward.

In cylindrical coordinates (R, ϕ, z), angular momentum conservation is given by (*11*)

$$\frac{\partial(2\pi R\Sigma j)}{\partial t}+\frac{\partial(\dot{M}_{\rm acc}j)}{\partial R}+\frac{\partial}{\partial R}\left[2\pi R^2\int_{z_{\rm bot}}^{z_{\rm top}}dz\left(\overline{\rho\delta v_R\delta v_\phi}-\frac{\overline{B_R B_\phi}}{4\pi}\right)\right]+ 2\pi R^2\left(\overline{\rho v_z v_\phi}-\frac{\overline{B_z B_\phi}}{4\pi}\right)\Bigg|_{z_{\rm bot}}^{z_{\rm top}}=0 \quad (1)$$

[1]Department of Earth, Atmospheric, and Planetary Sciences, Massachusetts Institute of Technology, Cambridge, MA, USA. [2]Institute for Advanced Study and Department of Astronomy, Tsinghua University, Beijing, China. [3]Department of Earth and Planetary Sciences, Harvard University, Cambridge, MA, USA.
*Corresponding author. Email: bpweiss@mit.edu (B.P.W.); xbai@tsinghua.edu.cn (X.-N.B.)

where we take the disk to be bounded vertically between vertical locations z_{bot} and z_{top}, Σ is the disk surface density, $j = \Omega_k R$ is the specific angular momentum at radius R, Ω_k is the Keplerian angular velocity, $\dot{M}_{acc}$ is the accretion rate (defined as negative for inward flows), $\boldsymbol{B} = (B_R, B_\phi, B_z)$ is the magnetic field, $\boldsymbol{v} = (v_R, v_\phi, v_z)$ is the local velocity of disk material, the symbol δ represents deviation from mean flow velocities, and the overbar indicates time and spatial averages. [We use centimeter-gram-second units in the main text of this paper and have listed Système International (SI) versions of the equations in the Supplementary Materials (note that 1 G = 100 μT)]. The first two terms represent the rate of change of angular momentum of disk material per unit radius and the net flow of angular momentum at radius R associated with accretion flows, respectively. The terms in the two parentheses in the third and fourth terms correspond to the $R\phi$ and $z\phi$ components of the stress tensor $\mathcal{T}$, representing the angular momentum flux transported along the R and z directions, respectively. Angular momentum transport can be of hydrodynamic (first terms in each parenthesis) and/or magnetic (second terms in each parenthesis) in origin. These terms are known as the Reynolds stress and Maxwell stress, respectively. Note that although there is also a contribution from self-gravity, we have ignored this for brevity and because it is likely important only in the earliest phases of disk formation.

Contribution from positive $\mathcal{T}_{R\phi}$ transports angular momentum radially outward, causing the inner disk region to lose angular momentum and accrete onto the protostar, whereas the outer disk gains angular momentum and expands. It is custom to parameterize the stress tensor as $\mathcal{T}_{R\phi} = \alpha P$, where P is the pressure and α is a dimensionless constant, resulting in the so-called α-disk model (*12*). In steady state with $\dot{M}_{acc}$ constant in radius and assuming an isothermal equation of state, $P = \rho c_s^2$, for isothermal sound speed c_s, one sees that the accretion rate is $\dot{M}_{acc} = 2\pi\alpha\Sigma c_s$. For a standard minimum mass solar nebula (*13*) disk model with surface density $\Sigma = 1700\ \mathrm{g\ cm^{-2}}\ (R/\mathrm{AU})^{-3/2}$ and temperature $T = 280\ \mathrm{K}\ (R/\mathrm{AU})^{-1/2}$, one finds $\dot{M}_{acc} \sim 8.3 \times 10^{-8} M_\odot \mathrm{year}^{-1} (\alpha/0.01)\,(R/\mathrm{AU})^{-1/2}$. Thus, a typical PPD accretion rate of $10^{-8}\ M_\odot \mathrm{year}^{-1}$, if solely driven by radial transport, generally requires $\alpha \sim 10^{-3}$ to 10^{-2}.

The effect of $\mathcal{T}_{z\phi}$ transports angular momentum vertically, carried out by a wind. Note that the hydrodynamic part of $\mathcal{T}_{z\phi}$ does not contribute to the net angular momentum loss because it simply describes the angular momentum of materials advected by the wind and thus does not extract extra angular momentum from the disk. Only the magnetic part of $\mathcal{T}_{z\phi}$ extracts additional angular momentum from the disk, which drives the entire disk to accrete. This illustrates that wind-driven accretion must be magnetic in nature.

From the above, we see that hydrodynamic mechanisms can contribute to radial transport of angular momentum. This is generally attributed to waves and turbulence and in particular requires correlated fluctuations in radial and azimuthal velocities (i.e., a positive $\overline{\rho\delta v_R \delta v_\phi}$ term). On the other hand, mechanisms involving magnetic fields can transport angular momentum both radially and vertically, for which turbulence is not necessary. Below, we briefly review our current understandings from both perspectives and conclude that magnetic mechanisms likely dominate.

Hydrodynamic turbulence

Overview

Hydrodynamic angular momentum transfer mechanisms generally rely on the onset and sustenance of turbulence, which is closely related to the hydrodynamic stability of the disk [see recent reviews (*14*, *15*)]. When ignoring thermodynamics, the stability of a disk is described by the well-known Rayleigh criterion (*16*), which states that a rotating, inviscid system is linearly stable to axisymmetric perturbations as long as j increases radially outward ($\partial j/\partial R > 0$) (Fig. 1) (*17*). In particular, consider a particle of mass M on a circular orbit, initially at position R_0 with initial specific angular momentum $j_0 = \Omega_0 R_0^2$ and angular momentum Ω_0. Because of angular momentum conservation, the parcel experiences an effective potential that includes a centrifugal term $\Phi_{eff} = \Phi_G + j_0^2/(2R^2)$, where $\Phi_G = -GM/R$ and G is the gravitational constant. It can be shown that Φ_G has a minimum at $R = R_0$, meaning that a circular orbit is stable to small perturbations. Thus, the Rayleigh criterion holds for Keplerian disks.

Hence, studies of hydrodynamic disk instabilities typically fall into two categories. First, consider the subcritical transition to turbulence. It is well known that linearly stable flows may become unstable to developing turbulence at large Reynolds numbers, where the Reynolds number is defined as $Re \equiv LV/\nu$ for system size L, characteristic velocity V, and fluid kinematic viscosity ν (*18*). Triggering such a transition requires finite-amplitude fluctuations and is thus termed "subcritical." However, it is not yet clear whether such a transition occurs for Keplerian rotation profiles [see (*19*)]. An extrapolation of numerical simulations conducted up to $Re \sim 10^4$ in the Rayleigh-stable regime toward Keplerian rotation found the critical Reynolds number Re_c for such a transition to be on the order of 10^{10} or higher (*20*),

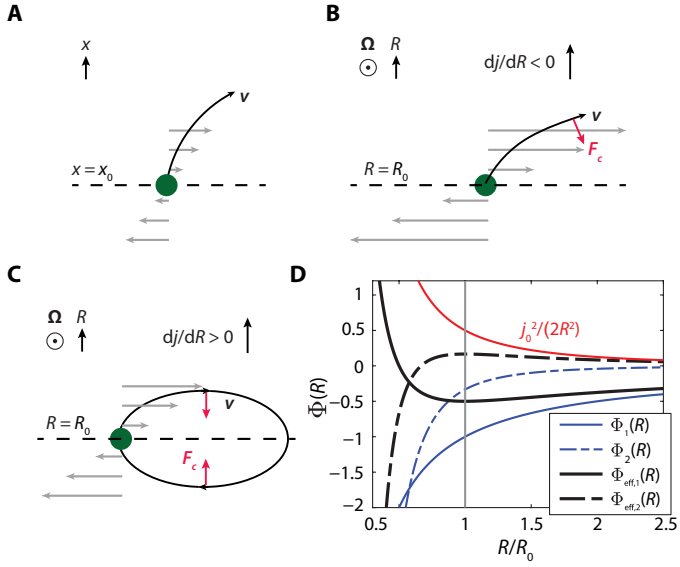

Fig. 1. Linear stability of accretion disks. Consider three flows with shears in fluid velocity, $\boldsymbol{v}$ (gray). (**A**) In a nonrotating flow, small displacements of fluid parcels (green) from initial position $x = x_0$ lead to unbounded motion (black curved arrow). (**B**) A rotating flow with angular velocity $\boldsymbol{\Omega}(R)$ for radius R in which the specific angular momentum $j = \Omega R^2$ decreases with R forms a strong shear such that despite the restorative influence of the Coriolis force $\boldsymbol{F_c} = -2\boldsymbol{\Omega}\times\boldsymbol{v}$ (red arrow), the motion is unbounded. (**C**) In a rotating Keplerian flow, $dj(R)/dR > 0$, leading to reduced shear compared to that of (B). As a result, the Coriolis force confines the motion into epicyclic trajectories (black loop). (**D**) Stability of a parcel on a circular orbit around $R = R_0$ (gray line) over two disk potentials $\Phi_1(R)$ [corresponding to (B)] and $\Phi_2(R)$ [corresponding to (C)], where $j_i(R) = \sqrt{R^3\, d\Phi_i/dR}$ (for i = 1, 2) increases with R for Φ_1 (as for a point mass potential) and decreases with R for Φ_2 (here more steeply than for a point mass). We have set $j_1(R_0) = j_2(R_0) \equiv j_0$. $\Phi_{eff,1}$ has a minimum at $R = R_0$ (motion is stable), whereas $\Phi_{eff,2}$ has a maximum at $R = R_0$ (motion is unstable). (A) and (C) after (*17*).

which is comparable to the typical Reynolds numbers of PPDs. However, upon transition to turbulence, the Reynolds stress scales as Re_c^{-1} such that the aforementiond high value of Re_c essentially makes angular momentum transport negligible.

Second, in recent years, several hydrodynamic instabilities have been discovered after considering more realistic disk thermal structures. Assuming adiabatic perturbations, the linear stability of a rotating disk subject to axisymmetric perturbations is described by the so-called Solberg-Høiland criteria (*14*, *15*, *21*), which combine the Rayleigh criterion with the Schwarzschild criterion that convection is driven by a positive entropy gradient. The Solberg-Høiland stability criteria are usually well satisfied in PPDs. However, the criteria may not be applicable because PPDs are not necessarily adiabatic: Gas is heated mainly by stellar irradiation, while sufficiently rapid cooling brings gas to equilibrium temperatures on time scales much shorter than the orbital time scale such that the gas is locally isothermal. Only in the opposite limit of slow cooling is the adiabatic regime relevant. Real disks are likely in between these regimes, having different cooling times in different regions depending on physical properties like the local disk structure and dust abundance.

Candidate hydrodynamic instabilities

Three purely hydrodynamic instabilities have recently been considered for PPDs: the vertical shear instability (VSI), the related processes of convective overstability (COS) and subcritical baroclinic instability (SBI), and the zombie vortex instability (ZVI). A detailed discussion for each of the instabilities is beyond the scope of this review; readers are referred to (*14*, *15*) for further information. Here, we summarize the main requirements for each instability to operate, their possible existence in PPDs (see Fig. 2), and the likely outcomes.

The VSI draws its free energy from the vertical gradient of azimuthal velocity v_ϕ. This vertical shear arises because, with stellar irradiative heating, the radial pressure gradient in the disk generally varies with height. The VSI requires the gas to be close to locally isothermal (i.e., having a cooling time scale shorter than ~1% of the local orbital time), a condition that is likely satisfied in a radial range of about 10 to 100 AU (*22*). Simulations show that the VSI leads to vigorous turbulence dominated by vertical motion. It achieves α values up to 10^{-3} in the limit of instantaneous cooling (*23*) and α values of several times 10^{-4} for more realistic cooling rates (*24*).

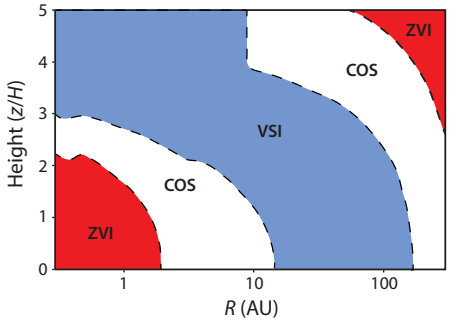

Fig. 2. Regions in the disk where various hydrodynamic instabilities may operate. Shown are the estimated locations where each of three hydrodynamic instabilities—the VSI (blue), COS (white), and ZVI (red)—is expected to dominate based on cooling time calculations for a specific disk model and under the assumption that magnetic fields are not present. Adopted from (*15*) with permission.

These fall short of the 10^{-2} value required for them to dominate angular momentum transport in outer disks.

The COS derives its free energy from a radial entropy gradient similar to convection (*25*, *26*). While radial convection is inhibited by disk rotation, the COS is achieved by allowing thermal relaxation so that epicyclic oscillations are boosted by buoyancy (*27*). The COS is most efficient when the cooling time scale is comparable to the orbital time scale. The nonlinear saturation of the COS is the SBI [a process actually discovered earlier (*28*, *29*)], which amplifies existing vortices over hundreds of orbital time scales. The vortices launch density waves that transport angular momentum outward with α values of up to a few times 10^{-3} (*29*, *30*). The result strongly depends on the outward radial entropy gradient, which, in typical models within 20 AU, is likely present mainly in the disk upper layer (rather than the midplane region where it would be more effective) (*15*).

The ZVI derives from the finding that vortices in stably stratified disks can excite "baroclinic critical layers" at some distance via buoyancy waves, which subsequently create copies of themselves (*31*, *32*) that eventually lead to turbulence with volume-filling vortices. The ZVI is a nonlinear instability that requires a finite-amplitude vorticity field to be triggered. It also requires the gas to behave nearly adiabatically (i.e., have a relaxation time of $\gtrsim$10 orbital times) such that the regions in which it may operate are primarily limited to the very optically thick inner ~1 AU of PPDs (*33*). Numerical studies so far are limited to local simulations, the contribution to angular momentum transport is likely small, and the associated Reynolds stress is well below the desired level (*34*).

In addition to the above processes, there is also the well-known gravitational instability (GI) (*35*). The GI is triggered when the Toomre Q value (*36*) $Q \equiv c_s\Omega/(\pi G\Sigma)$ falls below unity, possibly leading to very efficient angular momentum transport by spiral density waves and shocks (*37*). However, the onset of the GI requires a high surface density, which, if present, likely occurs only in the very early phases of PPDs [e.g., (*38*, *39*)]. Spiral density waves and shocks can also be generated from a massive outer companion [e.g., (*40*)] to which angular momentum can efficiently transported when the density jump across the shock approaches order unity (*41*); however, this scenario is unlikely to be applicable to the solar nebula as Jupiter is unlikely to have accommodated the angular momentum of the entire solar nebula (which is expected to be more than 10 times more massive than Jupiter and extending well beyond Jupiter's orbit). Recent high-resolution disk surveys have reported a paucity of spiral patterns (*5*, *6*), consistent with the general absence of GI in the bulk disk population. Another possibility is the Rossby wave instability (*42*), which is triggered in localized regions such as pressure extrema or disk gap edges. Although the Rossby wave instability tends to develop into large-scale vortices in the vicinity of such regions (*43*, *44*), it is unlikely to affect angular momentum transport at the global scale.

To summarize, a range of pure hydrodynamic instabilities may operate in PPDs under certain thermodynamic conditions. While we do not fully understand whether they exist and, if so, their potential effects on PPDs, current studies tend to suggest that they either are not present for the bulk of the PPD lifetime or do not provide sufficient angular momentum transport to account for typical PPD accretion rates.

Magnetohydrodynamic mechanisms

Overview

Magnetic fields have long been thought to play an important role in the gas dynamics of PPDs (*45*), and mechanisms involving magnetic

fields are now thought to be primarily responsible for angular momentum transport in PPDs. As mentioned earlier, the magnetic field can contribute to radial and vertical transport of angular momentum via the $R\phi$ and $z\phi$ components of the Maxwell stress tensor, respectively. Even without knowledge of detailed disk microphysics, some important constraints can already be obtained relating accretion rates and magnetic field strength (*46*, *47*).

More specifically, if accretion is mainly driven by radial transport through the $R\phi$ component of the Maxwell stress, we have $\dot{M}_{\rm acc} j = 2\pi R^2 L_z(\overline{B_R B_\phi}/4\pi)$, where the overbar again indicates time and spatial averages and L_z is the total thickness over which the stress is exerted [e.g., on the order of a few scale heights, $H \equiv c_s/\Omega_k$ (*48*), with $H \sim 0.03$ AU at 1 AU for a Sun-like star]. B_ϕ is expected to be the dominant field component because any radial field is easily sheared to produce B_ϕ. Ignoring B_z and assuming that, on average, B_ϕ is a factor $f > 1$ larger than B_R, we obtain [analogously to equation 16 of (*47*)]

$$B_{{\rm mid},R\phi} \cong 0.72{\rm G}\,(M/M_\odot)^{1/4}\left(\dot{M}_{\rm acc}/10^{-8}M_\odot\,{\rm y}^{-1}\right)^{1/2}(fH/L_z)^{1/2}\,(R/{\rm AU})^{-11/8} \quad (2)$$

where $B_{\rm mid}$ is the midplane field. Taking $f \sim 50$ and $L_z \sim 6H$ (see the "Relating paleomagnetic measurements to astrophysical constraints" section), one finds that the prefactor becomes 2.0 G.

On the other hand, if accretion is mainly driven by vertical transport (via a magnetized disk wind emerging from the disk surface), then assuming symmetry about the disk midplane, one finds that $\dot{M}_{\rm acc} j = 8\pi R^3 |\overline{B_z B_\phi}/4\pi|_{\rm base}$, where the subscript indicates the field strength at the base of the wind (usually several scale heights above and below the midplane). Similarly, assuming that, on average, B_ϕ is a factor $f' > 1$ larger than B_z at the wind base, we obtain [analogously to equation 7 of (*47*)]

$$B_{{\rm mid},z\phi} = mB_{{\rm base},z\phi} \cong m(0.065{\rm G})\,(M/M_\odot)^{1/4}\left(\dot{M}_{\rm acc}/10^{-8}M_\odot\,{\rm y}^{-1}\right)^{1/2} f'^{\,1/2}(R/{\rm AU})^{-5/4} \quad (3)$$

where we further assume that the midplane field is some factor m of the field at the wind base. Taking $f' \sim 10$ (see the "Relating paleomagnetic measurements to astrophysical constraints" section), one finds that the prefactor becomes 0.21 G.

A few remarks are in order regarding the above relations. First, these results are fairly general and are independent of disk surface density. Radial transport only weakly depends on disk temperature (through H). Second, given similar field strength, vertical transport is more efficient than radial transport by a factor of R/H, which is due to the large lever arm (R) for wind-driven accretion, whereas the $R\phi$ stress is exerted only over the disk thickness $L_z \sim$ a few H. Third, while Eqs. 2 and 3 offer separate constraints on field strengths for the two mechanisms, Eq. 2 expresses field strength averaged over the bulk disk and Eq. 3 indicates surface field strength. Fourth, the two mechanisms can coexist such that Eqs. 2 and 3 would reflect their individual contributions to accretion rates. Fifth, unlike previous expressions relating field strength to accretion rate (*10*, *47*), Eqs. 2 and 3 are not lower limits but instead direct estimates of the field with uncertainties reflected in the factors of f, f', and m, respectively.

Magnetic mechanisms

The main physical mechanisms responsible for radial and vertical transport are the magnetorotational instability (MRI) (*49*) and magnetized disk winds (*50*), respectively. A basic understanding of these two mechanisms can be obtained from two physical processes.

The first is the decomposition of the Lorentz force per unit volume (*51*). In the ideal magnetohydrodynamic (MHD) limit (i.e., for well-ionized gas; see below), it is given by

$$\boldsymbol{F} = \frac{1}{c}\boldsymbol{J}\times\boldsymbol{B} = \frac{(\nabla\times\boldsymbol{B})\times\boldsymbol{B}}{4\pi} = \boldsymbol{\kappa}\frac{B^2}{4\pi} - \nabla_\perp\frac{B^2}{8\pi} = \boldsymbol{F_T} + \boldsymbol{F_P} \quad (4)$$

where $\boldsymbol{\kappa} \equiv \boldsymbol{b}\cdot\nabla\boldsymbol{b} = -\boldsymbol{R}_c/R_c^2$ is the curvature vector of the field with curvature radius R_c, $\boldsymbol{b}$ is a unit vector in the direction of $\boldsymbol{B}$, and $\nabla_\perp$ denotes the components of the gradient perpendicular to $\boldsymbol{B}$. The two terms on the right are the magnetic tension, $\boldsymbol{F_T}$, and magnetic pressure, $\boldsymbol{F_P}$, both of which are perpendicular to $\boldsymbol{B}$. Equation 4 shows that magnetic field lines tend to straighten (act against bending) and spatial variations in magnetic field strength exert a pressure that can expel gas toward weaker field regions.

The second physical process is that Keplerian shear in the disk constantly generates toroidal field from radial field. In the ideal MHD limit, the magnetic induction equation $\partial\boldsymbol{B}/\partial t = \nabla\times(\boldsymbol{v_K}\times\boldsymbol{B})$ (see below) for a Keplerian velocity profile, $\boldsymbol{v_K}$, yields $\partial B_\phi/\partial t = -(3/2)\Omega_K B_R$.

For the MRI, consider two fluid elements along a vertical field line that are located at different heights in the disk (Fig. 3A). If one element is slightly displaced radially inward, it will orbit slightly faster, while if the other is displaced radially outward, it will orbit more slowly. The radial field resulting from this displacement is then sheared to produce toroidal field. The curvature in this field builds up magnetic tension, attempting to bring the two elements back to their initial positions. The tension thus acts like a spring, with the tension growing as the two elements are increasingly separated. However, the torque resulting from the spring reduces/increases the angular momentum of the inner/outer element, making it spiral inward/outward. The process runs away, giving rise to the MRI. In ideal MHD, the growth of the MRI saturates by generating vigorous turbulence (*52*) that can transport angular momentum radially outward with typical values $\alpha \sim 10^{-2}$ in the absence of a net vertical field threading the disk (*53*). With a net vertical field, α at saturation increases with disk magnetization and can even reach order unity (*54*). Because the $R\phi$ Maxwell stress usually dominates over Reynolds stress by a factor of ~4 to 5, accretion under these conditions is mainly magnetically controlled.

Magnetized disk winds require the disk to be threaded by a net vertical (poloidal) field. Because parent molecular clouds are magnetized (*55*), their fields may have been inherited by the disks as they are likely dragged in and bent radially outward during cloud collapse (*2*). At the disk surface layer, shear in the disk constantly generates toroidal field from the radial component of the outward-bent poloidal field (but with opposite signs at the two disk sides), making the toroidal field increasingly stronger. This has two consequences (Fig. 3B). First, magnetic pressure gradually builds up and eventually pushes the gas away from the disk, launching a wind. Note that this interpretation applies when the vertical field is relatively weak like that in PPDs (*11*), in contrast to the originally-proposed bead-on-wire centrifugally driven wind that requires a strong vertical field (*50*). Second, the process that amplifies radial into toroidal field increasingly pinches the poloidal field lines in the disk against the direction of rotation. Magnetic tension associated with this pinched field exerts a torque on the disk that opposes disk rotation, thereby extracting disk angular momentum corresponding to the $z\phi$ component of the Maxwell stress. The property of the wind is primarily

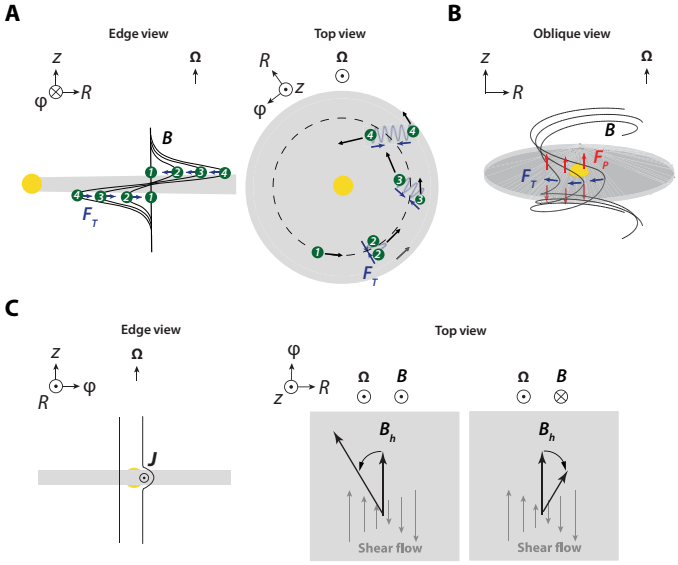

Fig. 3. Angular momentum transport by magnetic fields in a PPD. (**A**) The MRI. Shown is evolution at four different times (1 to 4). Left and right panels show edge-on and top views of disk. **Ω** denotes the direction of disk rotation. Grey denotes gas and yellow circle denotes the Sun (not to scale). 1: Two gas parcels (green) are initially located within a narrow annulus. 2: Displacement of one parcel inward and the other outward (black arrows in top view) decreases the outer parcel's angular velocity and increases that of the inner parcel. The field, ***B*** (black curves), then exerts a spring-like attractive force, $\boldsymbol{F_T}$ (blue arrows). 3 and 4: This continues to exert a torque on the parcels ($R\phi$ Maxwell stress) that causes them to further drift apart. This process runs away and eventually generates turbulence that also contributes to angular momentum transport via $R\phi$ Maxwell and Reynolds stresses. (**B**) The magnetized disk wind. The disk is initially threaded by a poloidal field. Keplerian shear of the radial field component produces a toroidal field. The Lorentz force associated with the vertical gradient of magnetic pressure, $\boldsymbol{F_P}$, launches a wind. The tension force, $\boldsymbol{F_T}$, from pinching of the field against the direction of rotation extracts angular momentum from the disk. (**C**) The HSI. Left: Starting with a vertical field, a perturbation in the ϕ direction creates a radial current ***J***, which yields a Hall drift velocity along the –***J*** direction. Right: When the initial field and disk rotation are aligned (left subpanel), this drift rotates the perturbed field counterclockwise in the plane of the disk, producing a radial field component. This radial field is then sheared to generate toroidal field that reinforces the initial perturbation, leading to angular momentum transport via $R\phi$ Maxwell stresses [e.g., right subpanel of (A)]. For an anti-aligned initial field (right subpanel), the Hall drift and shear reduce the initial perturbation. Right of subpanel (C) after (*48*, *72*).

controlled by the strength of the poloidal field threading the disk, with stronger field extracting angular momentum faster.

Complications from microphysics

Considering more physical details leads to substantial complications. PPDs are distinguished from other astrophysical accretion disks (e.g., black holes) in that they are extremely poorly ionized such that the coupling between gas and magnetic field is weak. This is because PPDs are generally too cold for collisional (thermal) ionization to occur unless temperatures exceed ~10^3 K (*56*). Instead, the bulk disk relies on nonthermal sources of ionization, particularly cosmic rays (*57*), stellar X-rays (*58*), and stellar ultraviolet radiation (*59*). The typical ionization fraction is of order 10^{-10} to 10^{-14} in the midplane at several AU and boosted to 10^{-4} to 10^{-5} in the disk atmosphere at a wide range of radii. Weakly ionized gas experiences nonideal MHD effects such that the magnetic field is no longer frozen into the fluid. There are three nonideal MHD effects: ohmic resistivity, the Hall effect, and ambipolar diffusion (AD) (*46*, *60*). Physically, they correspond to electron-neutral collisions, electron-ion drift, and ion-neutral drift, respectively, which allow field lines to drift relative to the gas and/or to dissipate in different ways. They are reflected in the nonideal MHD magnetic induction equation (*46*, *60*), which determines how magnetic fields evolve

$$\frac{\partial \boldsymbol{B}}{\partial t} = \nabla \times (\boldsymbol{v} \times \boldsymbol{B}) - \frac{4\pi}{c} \nabla \times (\eta_O \boldsymbol{J} + \eta_H \boldsymbol{J} \times \boldsymbol{b} + \eta_A \boldsymbol{J}_\perp) \quad (5)$$

where $\boldsymbol{v}$ is fluid velocity (i.e., velocity of the neutrals), $\boldsymbol{J} = (c/4\pi) \nabla \times \boldsymbol{B}$ is the current density, c is the speed of light, and the subscript $\perp$ represents the component perpendicular to $\boldsymbol{b}$. The three terms in the right parentheses are the ohmic, Hall, and AD terms, with corresponding magnetic diffusivities η_O, η_H, and η_A. The strength of nonideal MHD effects is characterized by the three Elsasser numbers, $\Lambda_{O,H,A} \equiv v_A^2/(\eta_{O,H,A}\Omega_K)$, where $v_A = B/\sqrt{4\pi\rho}$ is the Alfvén speed. These effects are considered strong when the corresponding Elsasser numbers are less than or equal to order unity. In most cases, it can be shown that $\eta_O \propto x_e^{-1}$, $\eta_H \propto x_e^{-1}(B/\rho)$, and $\eta_A \propto x_e^{-1}(B/\rho)^2$, where x_e is the ionization (i.e., electron) fraction. This specifies the relative importance of the three effects: Ohmic resistivity dominates in the densest regions (midplane of inner disk up to ~10 AU, where Λ_O is well below unity), AD dominates in the most tenuous regions [the surface layer of inner disk and the entire outer disk, where Λ_A is found to be of order unity (*60*)], and the Hall-dominated region lies in between.

Significant progress has been made in the past decade in understanding how individual nonideal MHD effects affect the local gas dynamics, particularly on the MRI, and the global dynamics when all these effects are combined with realistic ionization chemistry. A detailed description is again beyond the scope of this review. Here, we highlight some main results.

Ohmic resistivity is the best-studied. It suppresses the MRI when Λ_O falls below order unity (*61*). When only ohmic resistivity is considered, it creates a "dead zone" in the midplane region of the inner disk (*62*, *63*). AD can suppress the MRI for a strong field and damp the MRI for a weak field. The threshold field strength decreases with increasing AD (*64*). When ohmic resistivity and AD are combined, it is found that the MRI in the inner disk (~1 to 10 AU) is entirely suppressed in the disk vertical column (*65*). As a result, angular momentum transport requires the presence of a large-scale poloidal field threading the disk, which launches the magnetized disk wind. The wind is launched from the disk surface layer, where gas and magnetic fields are better coupled due to the higher level of ionization from stellar far-ultraviolet radiation (*65*, *66*). Note that because wind-driven accretion is highly efficient in angular momentum transport, only a weak net vertical field is needed to drive accretion at the desired rate of ~$10^{-8} M_\odot$ year^{-1}, corresponding to a plasma β (defined as the ratio of the gas pressure to the magnetic pressure) of the order 10^5 in standard solar nebular models. This picture likely also applies to the outer disk (beyond ~10 AU), which is entirely dominated by AD except that the outer disk can be weakly MRI turbulent (*67*, *68*)

Equation 5 shows that unlike in the ohmic or AD-dominated regimes, in the Hall-dominated regime (η_H significant compared to η_O and η_A), the field evolution depends on the polarity of the vertical disk field [this is also in contrast to the geodynamo, which is in the ohmic regime (*69*)]. When the net vertical field is aligned with disk rotation (i.e., $\boldsymbol{B} \cdot \boldsymbol{\Omega} > 0$), it results in the Hall-shear instability

(HSI), which strongly amplifies the horizontal (both radial and azimuthal) fields (*70–72*). In this context, the magnetic field has an effective drift (Hall drift) speed, $\boldsymbol{v}_H$, in the direction of $-\boldsymbol{J}$ as can be inferred from Eq. (5) (this is essentially the electron-ion drift speed). To understand the HSI, consider an initially vertical magnetic field in the disk perturbed in the ϕ direction (Fig. 3C). The Hall effect preserves the amplitude of the perturbed field and the Hall drift makes this pattern of magnetic perturbation rotate counterclockwise, producing a radial field component. The shear flow then generates toroidal field from the radial field that reinforces the perturbation, leading to instability. With both radial and toroidal fields amplified, the HSI yields a strong $R\phi$ Maxwell stress that leads to efficient radial transport of angular momentum. Unlike the MRI, the HSI itself does not generate turbulence and associated Reynolds stresses, although it can enhance turbulence if the MRI were active (*73–75*). In PPDs, the Hall effect is always accompanied by ohmic resistivity or AD, with the disk remaining largely laminar and launching disk winds. The wind also advects horizontal field out of the disk, which balances field growth and hence determines the saturation level of the HSI. As a result, contributions to angular momentum transport from $\mathcal{T}_{R\phi}$ and $\mathcal{T}_{z\phi}$ are typically found to be comparable. In the case of opposite polarity ($\boldsymbol{B}\cdot\boldsymbol{\Omega} < 0$), the Hall drift leads to clockwise rotation, and subsequent shear will generate toroidal fields that reduce the original perturbation. As a result, the horizontal field is reduced toward zero (*70*, *73*), thus contributing negligibly to angular momentum transport, although the configuration can be subject to a nonaxisymmetric instability that produces bursts of weak turbulence (*76*).

Theoretically, we anticipate that the initial conditions for star formation should not distinguish between the aligned and anti-aligned cases. However, it has been shown that the Hall effect also plays an important role during disk formation stage, resulting in different disk initial sizes depending on the polarity (*77*, *78*). Thus, disks with different magnetic polarities are likely born differently, although it is unclear whether such bimodality is present in observed disk populations. Hence, current theoretical studies treat the two cases as equally probable.

Recently, global disk simulations that incorporate all three nonideal MHD effects have been achieved (*79*, *80*). Figure 4 shows simulation snapshots under standard PPD parameters for both field-aligned and anti-aligned cases (*79*). It was found that in the aligned case, the horizontal field in the disk inner region (~1 to 10 AU) is amplified so much by the HSI that it does not change sign until reaching the surface at one side of the disk. Toward the outer region where the Hall effect (and hence the HSI) weakens, the change in sign occurs at the midplane. Transport of angular momentum by laminar Maxwell stress (radially) and by disk winds (vertically) makes similar contributions. For the anti-aligned case, the field configuration also shows a high level of asymmetry. The toroidal field is again the dominant field component, only changing sign at the very uppermost layer on one side of the disk. Without the HSI, the toroidal field is much weaker than for the aligned case. The bulk disk is weakly turbulent, although there are only minor spatial and temporal fluctuations in the total field strength that do not affect the overall field configuration (these fluctuations can be absorbed to the f or f' and m factors in

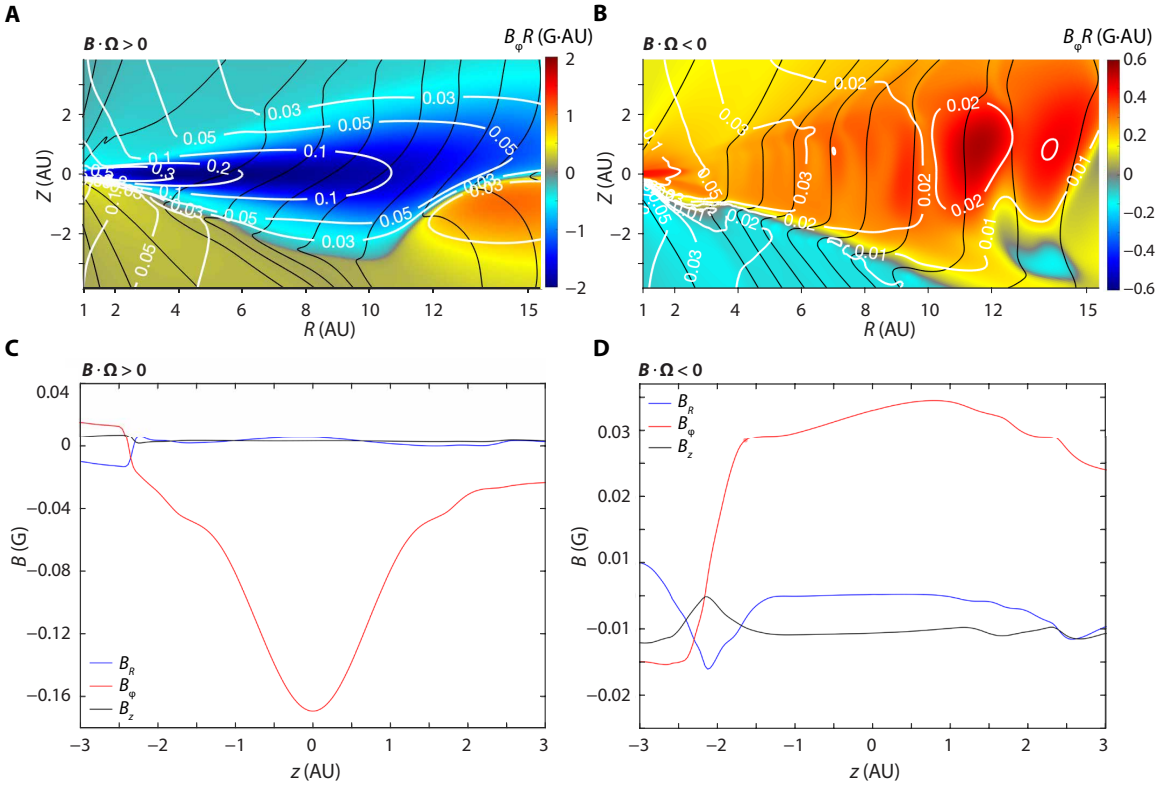

Fig. 4. Numerical simulations of the magnetic field evolution in a PPD. (**A** and **B**) Magnetic field configurations from two-dimensional axisymmetric simulations incorporating all nonideal MHD effects. (A) Vertical field aligned with disk rotation. (B) Vertical field anti-aligned with disk rotation. Shown in color is the scaled toroidal field strength (B_ϕ/Gauss)· (R/AU). Black contours mark poloidal field lines, and white contours mark the total field strength in Gauss. (**C** and **D**) Vertical profiles of the radial, azimuthal, and vertical components of the magnetic field at 7 AU from the simulations shown in the top panels for vertical field aligned (C) and anti-aligned (D) with disk rotation. Simulations from (*79*) after evolving about 1200 and 1800 years.

Eqs. 2 and 3). In both the aligned anti-aligned cases, the wind plays a major (if not overwhelming) role in driving disk accretion.

Relating paleomagnetic measurements to astrophysical constraints

As discussed below, an individual meteoritic sample (e.g., chondrule or bulk matrix sample) provides measurements of the paleomagnetic field strength. Accompanying information includes an estimate of the age and location (usually the midplane region at some radius) of the meteorite magnetic record, as well as the duration over which the magnetic record has been averaged (see the next section). Constraining solar nebula conditions requires that paleomagnetic measurements be understood in the context of a model of the nebular magnetic field. This can be achieved either by directly comparing with the best available PPD simulations or by using the more general relations Eqs. 2 and 3. Direct comparison with simulations has the advantage of having access to information about the entire radial and vertical profiles of magnetic fields (as in Fig. 4). However, the physical parameters of the primordial solar nebula are poorly known. On the other hand, Eqs. 2 and 3 are the most general but require proper understanding of the physical mechanisms that drive disk angular momentum transport and depend on physical parameters of f, L_z, f', and m.

The best understanding may be to combine both approaches, where we start from the framework of Eqs. 2 and 3 and quantify the uncertainties in the predicted value of B using the best-available simulations. Below, we discuss the situation in the inner disk (i.e., $R \lesssim 10$ AU). On the basis of recent simulations incorporating all nonideal MHD effects, it is found that when the net vertical field is aligned with the disk rotation, the midplane field is dominated by B_ϕ, which is amplified to order 10^2 times B_z, while B_R and B_z are comparable in strength. At the wind-launching region, B_ϕ is about a factor of 10 times B_z. In the anti-aligned case, $B_\phi \sim 10B_z$ throughout the disk (from the midplane to the wind base). Because wind-driven accretion dominates, we may use Eq. 3 and take $f' \sim 10$ for a rough estimate of the wind base toroidal field for both cases. In addition, we may take $m = 10$ and 1 for aligned and anti-aligned cases, respectively. For the aligned case, given that radial transport also makes significant contributions, we may also use Eq. 2, taking $f \sim 50$, $L_z \sim 6H$, which yields a field strength similar to the estimate from Eq. 3 at 1 AU. Simulations suggest that varying the fiducial parameters (e.g., surface density, magnetization, thermodynamics, and ionization and diffusivity models) modestly changes these ratios. These variations can lead to changes in f, L_z, f', and/or m in Eqs. 2 and 3 by a factor of a few such that we estimate an overall factor of up to ~3 uncertainty in the field strength from these considerations.

Three additional issues are worth mentioning. First, there may be modest localized spatial variations in the field. In particular, B_ϕ must change sign and go through zero when traversing vertically across the disk, at which location the disk field largely consists of just the vertical component. This means that the field values predicted from Eqs. 2 and 3 would be overestimates within a narrow range of disk heights. This may be more of an issue in the outer disk where the current sheet likely lies around the midplane (see also Fig. 4). The net vertical magnetic field may also be subject to localized radial variations on scales of a few times H superimposed on the general radial trend (*81*, *82*), although the variation may be more modest for total field strength. The total field strength may also vary in response to local variations such as condensation fronts (*82*) and, probably more importantly, from planet formation (although the latter has not been well quantified). Although the uncertainty associated with such spatial variations can be considered as different realizations of the previously mentioned uncertainties and hence can be readily absorbed into the uncertainty associated with the factors f, f', and m, here, we conservatively increase the uncertainty in field strength from the aforementioned factor of ~3 to now a factor of ~5.

Second, the background field may experience temporal variations that could be recorded by quickly-cooled meteoritic materials as a range of paleointensities that are individually snapshots of the field. Although existing global simulations have been run only up to a few thousand years, it appears that at least in the inner disk, no significant changes (e.g., in the direction of B_ϕ) occur other than some secular changes in total field strength from the slow, long-term evolution of magnetic flux. Therefore, the time-averaged (over at least >1000 years) and instantaneous field strengths at a given location in the disk are expected to be similar.

Third, if the meteoritic object (e.g., chondrule) is itself spinning rapidly relative to the field variations, then it will record the projection of the background field on the body's spin axis, which will, on average, reduce the apparent paleointensity by a factor of 2 for a population of bodies with randomly oriented but non-tumbling spin axes (*83*). The uncertainty associated with this effect can be reduced to a negligible level if a sufficient number of paleomagnetic measurements are measured and averaged from chondrules formed within a restricted location and time window.

Additional uncertainties arise from the disk accretion rate. Astronomical observations can only measure instantaneous accretion rates onto the protostar that are not necessarily the same as the accretion rate at a certain radius. Furthermore, the measured stellar accretion rates are typically uncertain by a factor of 2 to 3. Individual disks can also differ significantly from each other, and there is an overall trend that accretion rate decreases with age, reaching up to $10^{-6}\ M_\odot$ year^{-1} at the youngest ages (in the so-called class 0 phase in the first ~10^5 years), down to well below the standard value of $10^{-8}\ M_\odot$ year^{-1}. In particular, disks with young ages ($\lesssim$1 Ma) likely experience FU Orionis–like (typically class 0) or EXOr-like (typically class I/II) outbursts, which are interpreted as episodic boosts of the accretion rate by a factor of up to a few hundred or up to a few tens, respectively (*84*). Our ignorance about nebular accretion rates limits the use of paleointensities to constrain nebular physics. A median value of ~$10^{-8}\ M_\odot$ year^{-1} for a 1 $M_\odot$ star is a reasonable estimate for the bulk lifetime of the solar nebula (i.e., class II phase), modulo uncertainties by up to a factor of a few. Given that the field strength depends on the square root of the accretion rate (see Eqs. 2 and 3), this uncertainty is ~$3^{1/2}$, unless we are considering the accretion rates at the very early phases of the solar nebula or near the end of disk lifetime. Combining all of the above uncertainties (i.e., associated with the factors of f, L_z, f', and m; spatial variations of the field; and accretion rate), we estimate that at most times and locations in the disk, the total uncertainty on the predicted field as a function of distance is less than or equal to an order of magnitude.

These uncertainties apply to predictions of the nebular field strength from theory and simulations to compare with measured paleointensities. Conversely, as discussed below, paleointensity measurements can be used to constrain accretion rates or the formation location of the meteorites, with uncertainty factors again propagating according to Eqs. 2 and 3.

Multiple constraints can help reduce uncertainties. For example, multiple paleomagnetic measurements from samples originating from different heliocentric distances and different ages can be considered

collectively in the context of the theory. In the meantime, astronomical observations of young PPDs are also on the verge of providing useful constraints to disk magnetic fields, as we discuss next.

ASTRONOMICAL OBSERVATIONS

As mentioned earlier, disk magnetic fields are likely inherited from the star formation process. The existence of magnetic fields in molecular clouds and protostellar cores is well established [see (*55*) for a review]. This was achieved mainly through two techniques: observations of dust polarization and of the Zeeman effect.

In the interstellar medium (ISM), any irregular-shaped dust grain in an anisotropic radiation field can be spun up around its short axis. The spinning grain can then acquire a magnetic moment along this axis due to surface charges and/or the Barnett effect (in which a spinning body with unpaired electrons can spontaneously acquire a magnetization proportional to the rotation rate) (*85*). In the presence of a magnetic field, its spin axis will then precess around the magnetic field and eventually align with the field due to dissipation [e.g., (*86*)]. Once aligned, dust extinction of initially unpolarized background light after passing through the dusty region would be strongest for polarization oriented perpendicularly to the sky-projected field orientation, $\boldsymbol{B}_{\mathrm{POS}}$. This means that background starlight should exhibit linear polarization along $\boldsymbol{B}_{\mathrm{POS}}$. On the other hand, thermal emission from the dust (mostly at wavelengths comparable to or longer than the dust grain size) is primarily linearly polarized along the long axis that is perpendicular to $\boldsymbol{B}_{\mathrm{POS}}$. Observations of both kinds of emission are extensively used to study magnetic fields in the ISM and star-forming regions and have revealed a link between magnetic field orientations, gas densities, and kinematic structures on a variety of scales [see (*87*–*89*)].

The Zeeman effect describes the splitting of spectral lines into multiple components of slightly different frequencies in the presence of a magnetic field. The amount of splitting is proportional to B. However, for the ISM field strength, the splitting is usually too small to be spectrally resolved, such that its effect is mainly exhibited as circular polarization whose polarization degree is proportional to the line-of-sight component of the field, B_{LOS}. In the ISM, the Zeeman effect has been detected in atomic H, OH, and CN lines, as well as in masers, all in submillimeter to radio wavelengths. These measurements have measured field strengths over a wide range of densities from ~10 μG from diffuse clouds to up to a few mG in molecular cores [e.g., (*55*)].

Primarily, efforts to measure magnetic fields in disks have focused on measuring polarized dust continuum emission, which is expected to largely probe the disk midplane region (for optically thin dust) and also to sense the surface of edge-on systems. This approach is challenging partly because disks are small (about 10^{-3} the size of molecular clouds and 10^{-2} the size of prestellar cores), and hence, resolution and sensitivity requirements are highly demanding. Early attempts yielded either only upper limits (*90*, *91*) or positive detections whose inferred field configuration is somewhat puzzling under the assumption of magnetic alignment (*92*–*94*).

With respect to theory, because of grain growth and the fact that gas in PPDs is much denser than that in the molecular cloud, it is likely that dust spin becomes collisionally damped before it can precess around the magnetic field toward alignment (*95*, *96*). In addition, several mechanisms have been proposed to produce submillimeter continuum polarization without involving magnetism. In particular, it has been realized that thermal emission from submillimeter-sized dust can be scattered by other dust (called self-scattering) to yield linearly polarized radiation (*97*, *98*). The polarization pattern and polarization fraction depend on disk inclination and can be used to constrain dust properties.

The situation has been revolutionized with the advent of the Atacama Large Millimeter/submillimeter Array (ALMA). With orders of magnitude improvement in resolution and sensitivity, it has enabled spatially-resolved measurements of linear polarization pattern for nearby PPDs. More than a dozen disks have been observed so far, showing polarization intensities and orientations in the majority of cases that are consistent with self-scattering (*9*, *99*, *100*). However, the situation is more controversial for some observations at longer wavelength of 3 mm (*101*, *102*), pointing to other mechanisms such as radiative alignment (*96*) and aerodynamic alignment (*103*), although these interpretations are also not without problems (*104*). In addition, polarization in two young and edge-on systems appears to be consistent with multiple origins, and magnetic dust alignment remains compatible with the data (*105*). Overall, there is a paradigm shift in the disk community that dust continuum polarization has a commonly nonmagnetic origin, but the detailed mechanisms are still under active research.

Recently, ALMA has opened up the possibility of measuring circular polarization, and it has become possible to constrain the line-of-sight field strength via the Zeeman effect. Modeling suggests that using the CN line [which is likely the most sensitive tracer of the surface layer and outer region (*106*)], a positive detection requires an area-averaged mean line-of-sight field strength of the line-emitting region to be at least 1 to 10 mG given the current sensitivity of ALMA (*107*). Given the required sensitivity, typical spatial resolutions would be at least several tens of AU for disks in nearby star-forming regions. So far, several observational studies are being conducted, but no positive detection has yet been reported (*108*). The fact that the disk magnetic fields are likely smooth (as the MRI is largely suppressed) minimizes cancellations along the line of sight. In the meantime, on the basis of the discussion above, we anticipate younger disks with higher accretion rates (exceed $10^{-8}\ M_{\odot}\ \mathrm{year}^{-1}$) to be promising candidates.

In addition to the above, molecular line emission (i.e., rotational transitions) can become linearly polarized either parallel or perpendicular to the magnetic field due to the Goldreich-Kylafis (GK) effect (*109*). The GK effect results from the magnetic sublevels of the excited state deviating from local thermodynamic equilibrium due to an anisotropic radiation field, which can be external or internal in origin (e.g., from an anisotropic velocity gradient). It can be used to map out the orientation (but not intensity) of the plane-of-sky magnetic field, but there is a 90° directional ambiguity. The GK effect has been detected in evolved stars (*110*) and star-forming regions including molecular outflows (*111*, *112*). Forward modeling suggested that the effect can potentially be detected in PPDs (*113*). Very recently, marginal detections toward two disks by ALMA have been reported (*114*), although the data are insufficient to infer field morphology.

PALEOMAGNETISM

Introduction

Natural remanent magnetization

A unique opportunity to study nebular magnetism is offered by our solar system, for which we have planetary materials that recorded

ancient magnetic fields. Their record is in the form of NRM, a macroscopic vector quantity that reflects the semipermanent alignment of electron spins. NRM in planetary materials can, in principle, persist for far longer than the age of the solar system, long after the decay of the magnetizing field (*115*).

Paleomagnetic records from solar system materials are obtained from laboratory analyses of meteorites and in situ spacecraft magnetometry of small bodies. Paleomagnetic studies are complementary with respect to astronomical observations for characterizing nebular magnetism. Meteorite studies probe the conditions in our own well-studied early solar system, while astronomical studies can characterize a diversity of young stellar objects. Furthermore, as mentioned above, paleomagnetic measurements likely constrain the field in the midplane where planetesimal formation and radial-azimuthal accretion occur, while astronomical observations using the Zeeman effect would mainly provide area-averaged line-of-sight field components of the line-emitting region, likely tracing the disk surface.

Meteorite studies have four principle advantages over astronomical observations. First, paleomagnetic measurements constrain fields at extremely high spatial resolutions (down to the 0.1-mm or smaller scale of chondrules and inclusions). Second, unlike the model-dependent field strengths for dust polarization studies, they enable direct and highly accurate measurements of field paleointensities (in principle, up to 10% or better). Third, paleointensities typically have very highly accurate and precise ages (with uncertainties as little as 0.1 Ma) due to the ability to date the samples using radiometric methods. Fourth, because meteoritic materials have acquired their NRMs over time scales ranging from hours to millions of years or longer depending on the sample, they can probe the time-averaged field over a wide range of time scales along with the instantaneous field measured astronomically.

On the other hand, there are several disadvantages of paleomagnetic studies relative to astronomical observations. First, because the original orientations of meteoritic materials in the nebula are unknown, only the field paleointensity and not its paleodirection can be inferred. Second, the locations at which planetary materials acquired their NRMs may be difficult to constrain. Third, meteoritic materials may have been derived from only a small fraction of the volume of the solar nebula whose local conditions might not reflect the mean state of the overall disk.

Small bodies and meteorites with paleomagnetic records dating back to the early solar system are thought to mainly contain one of four forms of NRM when they cool, crystallize, or accrete in the presence of a steady ambient paleomagnetic field, B_{paleo}. Igneous materials (e.g., chondrules) and thermally-metamorphosed materials acquire a thermoremanent magnetization (TRM) during cooling below the Curie temperature of their constituent ferromagnetic minerals (*116*). Materials in which ferromagnetic crystals grow and/or experience recrystallization at low temperatures acquire a crystallization remanent magnetization (CRM) (*116*). Both TRM and CRM have been identified in a diversity of meteorites. Compression-decompression cycles due to impacts may have also imparted shock remanent magnetization (SRM), although such magnetization has not yet been unambiguously identified in natural samples (*117*). Last, it has recently been proposed that meteoritic materials could acquire an accretional detrital remanent magnetization (ADRM) resulting from compass-needle alignment of their constituent grains during gentle accretion (*118*). Although ADRM has not yet been recognized in meteorites, its terrestrial counterpart, known as detrital remanent magnetization, is ubiquitously observed in clastic sediments on Earth.

For typical geologic and meteoritic materials, NRM is approximately proportional to the intensity of the ancient magnetizing field for the typically weak ($\lesssim$10 G) fields expected in the nebula (*116*)

$$M_{NRM} = \chi B_{paleo} \tag{6}$$

where M_{NRM} denotes NRM and χ is the remanence susceptibility, a constant that depends on both the nature of ferromagnetic grains in the sample and the form of magnetization.

To obtain B_{paleo} from laboratory paleomagnetic measurements, M_{NRM} is measured after removing any partial magnetization overprints by degaussing and/or heating the sample in zero field. Then, because χ is not known a priori, the sample is remagnetized in a known laboratory field, B_{lab}, followed by measurement of the resulting magnetization, M_{lab}. Assuming that χ remains unchanged by this process, the two resulting equations can be divided to obtain $M_{NRM}/M_{lab} = B_{paleo}/B_{lab}$ and solved for B_{paleo} (*116*). In principle, this requires that M_{lab} have the same form of magnetization (i.e., TRM, CRM, SRM, or ADRM) as M_{NRM} because each form of magnetization will have a different value of χ. However, reproducing the magnetization process for ADRM and most forms of SRM and CRM is currently essentially impossible in the laboratory given the unknown conditions in which these forms of magnetization were acquired by meteorites and the difficulty of recreating such conditions even if they were known. This is far more straightforward for obtaining paleointensities from natural TRMs, which involves heating and cooling the samples in the laboratory. Even so, even such heating experiments are challenging because they can cause the samples to undergo thermochemical alteration that leads to changes in χ. To alleviate the requirement that the laboratory remanence be produced by the same process that produced the NRM, a sample can instead be given an analog magnetization like saturation isothermal remanent magnetization (IRM) (exposure to a strong field at room temperature) or anhysteretic remanent magnetization (ARM) (exposure to an alternating field with superimposed DC bias field at room temperature); if the ratio of the χ value for IRM to that of TRM or for ARM to TRM is independently known [e.g., through calibration experiments on analog samples (*119*)], a paleointensity estimate can be obtained with typical uncertainties of between a factor of ~2 and up to an order of magnitude (*120–122*). Because CRMs usually have lower intensities than TRMs acquired in the same field (at least for ferromagnetic minerals that did not form as transformation products of preexisting ferromagnetic minerals), only a minimum paleointensity can usually be inferred from CRM-bearing meteorites (*123*).

Rock magnetism

Ferromagnetic minerals contain unpaired electron spins whose orientations are mutually coupled by quantum mechanical exchange interactions. Hence, they can form crystals with nonzero magnetic moments that can record an ambient magnetic field in the form of NRM. The most common ferromagnetic minerals in meteorites used for nebular magnetic field studies are the metals kamacite (α-$Fe_{1-x}Ni_x$ for $x < \sim0.05$), martensite (α_2-$Fe_{1-x}Ni_x$ for $\sim0.05 < x < \sim0.25$), and awaruite ($Fe_{1-x}Ni_x$ for $\sim0.67 < x < \sim0.75$); the iron oxide magnetite (Fe_3O_4); and iron sulfides like monoclinic pyrrhotite ($Fe_{1-x}S_x$ for $x < \sim0.13$) (*124–126*). Kamacite and martensite typically dominate the remanence of unmetamorphosed ordinary chondrites and most

basaltic achondrites, whereas magnetite and sulfides carry much of the remanence in carbonaceous chondrites as well as in some achondrites like angrites.

A critical requirement for successful paleomagnetic studies is the identification of samples with high-fidelity magnetic recording properties. This means that the samples should (i) have been capable of acquiring an NRM proportional to the paleofield as described by Eq. 1, (ii) be able to retain this magnetization over at least 4.5 billion years, and (iii) be able to be cleaned of overprinting remanence by laboratory thermal or alternating field (AF) demagnetization. It has long been recognized that materials with a significant fraction of crystals with sizes in the single domain range (whose electron spins are uniformly aligned within the grain) are optimal magnetic recorders in this way (*116*). However, for some ferromagnetic minerals like kamacite, the single domain size range can be vanishingly narrow for grains with equant shapes (*127*). As a result, FeNi-bearing meteoritic materials are instead commonly dominated by larger grains like those in the single vortex state (for which the spins typically take the form of a uniformly oriented core surrounded by a spiral structure). Nevertheless, very recent advances in micromagnetic modeling have now established that most single vortex grains can carry exceptionally high-stability NRM that can be stable over the history of the solar system (*128*).

Several different kinds of materials have recently been identified to likely carry high-fidelity records of nebular fields. In particular, a small fraction of chondrules (typically 10% in ordinary chondrites and even rarer in carbonaceous chondrites) contain submicrometer-sized crystals of nearly pure Fe kamacite embedded in forsterite called "dusty olivines" (Fig. 5). This metal is thought to have formed during a reduction process before accretion. The metal's fine grain size means that much of it is in the single vortex size range (*129*–*131*). Furthermore, its very low Ni abundance (<2 weight %) guarantees that the metal grains did not undergo subsolidus phase changes that can occur during slow cooling on the parent body long after accretion and that may alter the paleomagnetic record (*132*, *133*). Hence, dusty olivine-bearing chondrules that remained below the 780°C Curie point of kamacite following formation are almost certain to contain a total TRM record of nebular magnetism.

Another class of high-fidelity ferromagnetic minerals in meteorites are magnetite and pyrrhotite grains that typically formed during post-accretional aqueous alteration on the parent body. These grains may contain a CRM (for meteorites that remained at low temperature during and after metasomatism like CM chondrites) or a TRM for heated meteorites (like metamorphosed CM chondrites). Like dusty olivine metal, magnetite and pyrrhotite in meteorites commonly form grains in the single domain and single vortex size range, but they have the additional advantage of usually being much more resistant than FeNi to thermochemical alteration during laboratory heating (see above). Another limitation is that because magnetite and pyrrhotite typically usually formed after accretion of the parent body, it can be challenging to distinguish whether their NRMs were acquired in the nebular field or that of a dynamo generated within the meteorite parent body (*134*).

Remagnetization processes

A central challenge faced by paleomagnetic studies is to establish whether the NRM in a given sample formed in the early solar system in the presence of a nebular magnetic field or instead is a more recent overprint. Although atmospheric passage typically only thermally remagnetizes the outer <0.3 cm of stony meteorites, many meteorites are later essentially completely remagnetized by collector's hand magnets and weathering on Earth's surface (*125*, *135*). Furthermore, even those meteorites that avoided remagnetization on Earth may have already been remagnetized by thermal metamorphism, aqueous alteration, and/or phase changes and heating from impacts on their parent bodies following the dissipation of the nebula.

There are several ways that the age of the NRM can be established. Radiometric ages can constrain the timing of thermal and crystallization events. Petrographic and mineralogical analyses can constrain relative formation ages of ferromagnetic minerals based on their textures, compositions, and overprinting relationships with other materials in a meteorite. For example, sulfide veins that transect from a chondrule's interior into the surrounding matrix [as observed CV chondrites (*136*)] must postdate accretion. Furthermore, measurements of mutually oriented subsamples of a given meteorite can provide direct relative age constraints on the time of NRM acquisition (*137*). For example, the demonstration that the NRM direction in the fusion crust and adjacent baked interior zone is distinct from that of the deeper interior would indicate that the meteorite has not been completely remagnetized as part of a single remagnetization event after landing on Earth (*125*). Furthermore,

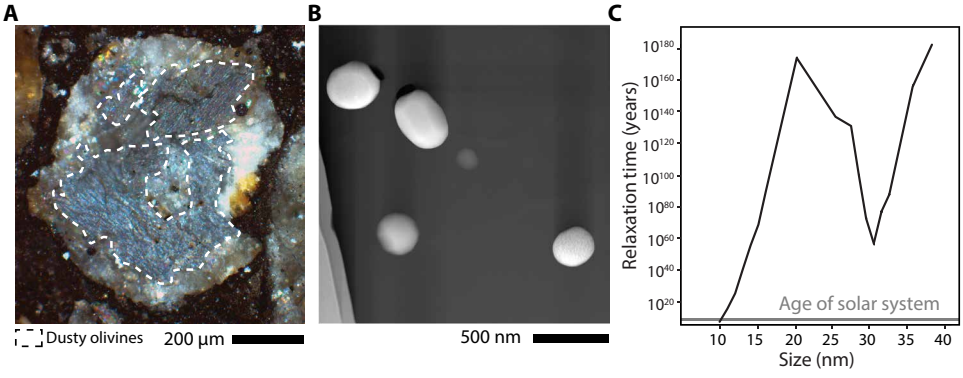

Fig. 5. Dusty olivines as carriers of nebular magnetization. (**A**) Reflected light optical photomicrograph of dusty olivine-bearing chondrule in the LL Semarkona meteorite. Light gray regions are mostly forsterite, whereas darker gray regions outlined by white dashed lines are rich in dusty metal. (**B**) Transmission electron microscopy image of four dusty olivine kamacite crystals (white ellipsoids) in forsterite (dark gray background). (**C**) Relaxation times at room temperature of kamacite cuboids with aspect ratios of 1.5 as calculated by micromagnetic modeling and compared to the age of the solar system (gray line). Grains larger than 25 nm in diameter are in the single vortex state, while smaller grains are in the uniform (e.g., single domain or flower) state. (A) and (B) after (*10*) and (C) after (*130*). Photo credit for (A): R. R. Fu, MIT.

because the nebular field is not expected to exceed ~5 G in most locations (e.g., Eqs. 2 and 3), a demonstration that the ratio of NRM to saturation IRM is <10% indicates that the sample has likely escaped exposure to a hand magnet (*122*, *125*, *138*). Last, the demonstration that relative magnetization directions of individual chondrules or other clasts and inclusions are collectively random (while each individual object has magnetization that is uniformly oriented within it) would indicate that their NRM predates assembly of the meteorite (*83*). For chondrules, which are expected to have accreted onto their parent body with orientations that are random relative to the paleofield direction (assuming no ADRM forms), the observation of scattered magnetization directions can be taken as powerful evidence that their NRMs formed before accretion.

Meteorite measurements

Overview

Although the paleomagnetism of meteorites has been studied since the 1950s (*139*), the nature and meaning of meteorite NRM have only begun to be understood in detail in the last decade. In particular, the identification of ferromagnetic minerals thought to have formed in the early solar system along with tests of NRM stability and age (see above) have recently enabled the identification of early solar system magnetic field records in four chondrite parent bodies (LL, CM, CV, and CR groups) and two achondrite parent bodies (angrites and NWA 7325). We now review the paleointensity records from these meteorites. We only discuss samples for which rock magnetic analyses, radiometric ages, and constraints on the remagnetization history have established that the NRM is ancient (e.g., no younger than 6 Ma after the formation of the solar system).

Ages of NRMs

The ages of the NRM records in these meteorites are precisely constrained by a variety of short- and long-lived radionuclide systems (table S1). Because we are interested in the ages of the field records relative to the formation of the solar system rather than their absolute ages, we have calculated ages relative to CAIs, which are the oldest known solids and which are thought to have formed within 10^5 years of the collapse of the molecular cloud (*140*). The meteorite materials used for dating are chondrules, secondary alteration minerals (magnetite and carbonate), and bulk igneous rocks (as well as separates from these materials). The crystallization, thermal metamorphism, and aqueous alteration events experienced by these materials have been dated using both the long-lived U-Pb system, which provides absolute ages, and several short-lived systems (Al-Mg, I-Xe, Mn-Cr, and Hf-W), which provide ages relative to a standard whose absolute U-Pb age is independently known (*141*). The use of relative chronometers relies on the assumption that the initial abundance of the short-lived parent nuclide was homogeneous in the solar system where the standard and the sample of interest formed. However, relative chronometers have the advantage over U-Pb ages in typically having higher precision due to the much shorter half-lives of their parent nuclides. A second advantage of the Al-Mg and Hf-W systems, in particular, is that CAIs themselves are commonly used as a standard, meaning that uncertainties associated with the absolute age of CAIs do not contribute to the uncertainty budget for these systems. This is relevant because estimating the uncertainty of an age relative to CAIs should not only include the nominal measurement uncertainties of any CAI age but also take into account the consideration that there are two different ages that have been obtained for CAIs, which differ from each other by >3 SDs: 4567.30 ± 0.16 Ma ago from (*142*) and 4567.94 ± 0.21 Ma ago from (*143*) (with the caveat that only the former age has been described in a detailed refereed publication).

Meteoritic materials acquired their NRMs over widely varying time scales. Therefore, their paleomagnetic records represent average magnetic fields over these time scales. Chondrules are thought to have typically cooled from the Curie point to ~0°C over time scales of ~1 to 10^3 hours (*144*–*146*) such that they acquired a near-instantaneous TRM record of the ambient field. By comparison, aqueous alteration of chondrites on their parent bodies is thought to have a duration of >1 year (*147*) and up to several Ma (*148*) such that post-accretional CRMs should provide a time-averaged record of the field that could extend over a significant fraction of the nebula's lifetime.

Locations where NRMs were acquired

There are broad constraints on the formation locations of meteoritic materials that enable interpretation of their magnetic records in the context of nebular processes. With respect to their vertical positions in the disk, drag forces on 0.1-mm-sized grains in the nebula may lead them to settle below a height H above the midplane at 1 AU from the Sun within ~10^4 years (*149*), consistent with observational evidence of settling and the largely laminar environment expected from theoretical considerations (see above) (*150*). Hence, it is expected (although not required) that most meteorites and their constituent chondrules and refractory inclusions should have recorded magnetic fields near the midplane. With respect to their radial positions in the disk, observations of meteoroid trajectories indicate that nearly all parent bodies were immediately derived from the asteroid belt (2 to 3 AU) (*151*). However, this does not require that the meteorites were in the present-day asteroid belt during their formation. In particular, it has recently been realized that known meteorites are derived from two groupings ("carbonaceous" and "noncarbonaceous") with distinct O, Cr, Ti, Mo, and W isotopic compositions that are thought to sample two nebular reservoirs [e.g., (*152*)]. It has been proposed that these two reservoirs were located within and beyond proto-Jupiter's orbit, respectively, where they had become isolated when proto-Jupiter opened up a gap in the disk after reaching its isolation mass. In particular, an analysis of the abundance of CAIs and refractory elements in meteorites has predicted that noncarbonaceous and carbonaceous parent bodies accreted at ~2 to 3 and 3 to 4 AU (*153*), whereas the similar oxygen isotopic compositions of ordinary and carbonaceous chondrites suggest formation of the latter within <7 AU (*154*).

Paleointensity results

We now summarize existing paleointensity constraints on the nebular field (Figs. 6 to 8 and tables S1 and S2). Measurements of chondrules from the Semarkona LL chondrite (*10*) indicate the existence of a near-instantaneous field of intensity 0.54 ± 0.21 G at ~1 to 3 AU (*153*) at 2.03 ± 0.81 Ma after the formation of CAIs (Fig. 6). If chondrules formed by nebular shocks associated with planetary bow shocks, then they are expected to record a field intensity similar to that of the ambient unshocked nebula (*155*). Because the LL chondrules in Semarkona are magnetized in random directions, they must have been magnetized before accretion and therefore recorded the nebular field (see the "Remagnetization processes" section).

Paleomagnetic studies of seven CM chondrites (*134*) indicate that they were magnetized by a field of >0.06 G at ~3 to 7 AU (*153*, *154*) at 2.90 ± 0.39 Ma after CAI formation (Fig. 6) (*134*). The NRMs within the CM chondrites are unidirectional and carried by

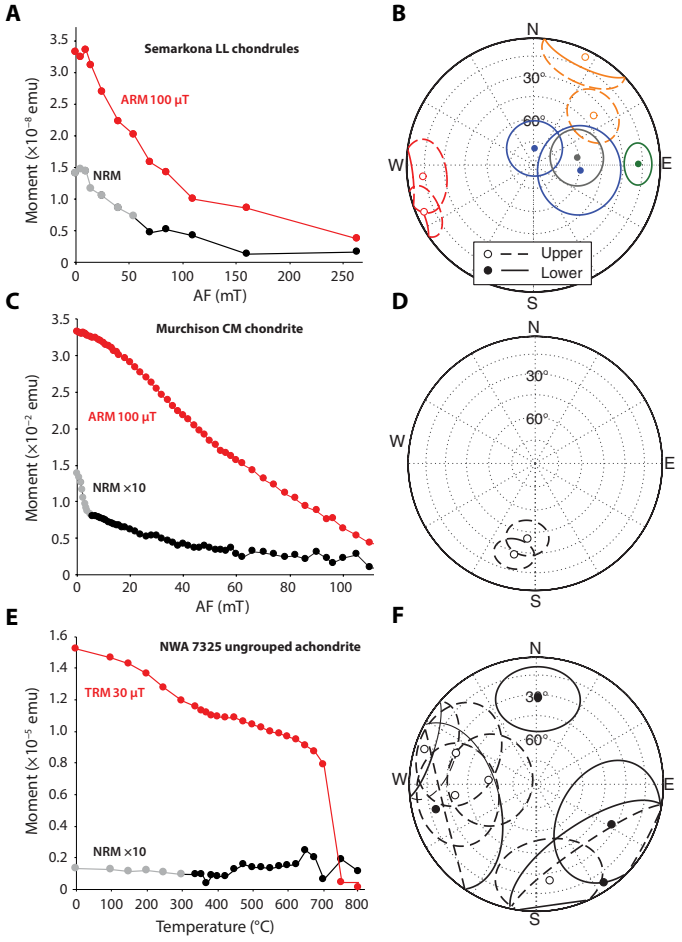

Fig. 6. The nebular magnetic field as recorded by meteorites. (**A** and **B**) Chondrules from LL chondrite Semarkona (*10*). (**C** and **D**) Bulk samples of CM chondrite Murchison (*134*). (**E** and **F**) Bulk samples of ungrouped achondrite NWA 7325 (*124*). (A, C, and E) Evolution of magnetic moment in electromagnetic units (emu) during AF or thermal demagnetization of NRM (gray and black symbols), ARM (A and C) (red symbols), and TRM (E) (red symbols). Grey symbols denote secondary NRM components and black symbols denote high-coercivity NRM components interpreted to be records of nebular field conditions. (B, D, and F) Equal-area stereonets showing the directions obtained from least-squares fits (circles) and associated maximum angular deviation values (ellipses; a measure of uncertainty) for the high-coercivity components in five chondrules (B), two bulk subsamples (D), and nine bulk subsamples (F). In (B), (D), and (F), open (closed) symbols and dashed (solid) lines denote upper (lower) hemisphere projections. In (B), individual chondrules are denoted by distinct colors, with three chondrules yielding two mutually oriented subsamples each. In (C) and (E), NRM is multiplied by 10 for visibility. ARMs were acquired with a 2900 G AC field and 1 G bias (A) and a 1000 G AC field and 1 G bias (B), while the TRM was acquired by heating to 800°C in a field of 0.3 G.

the magnetite-bearing aqueously altered matrix, requiring that they were magnetized after accretion. They should have recorded the time-averaged field, consistent with the difference between CM I-Xe and Mn-Cr ages (table S2). The post-accretional nature of the NRM in CMs means that the origin of the magnetizing field is somewhat ambiguous. It may have been a product of the nebular field or conceivably a more recent field like that of a core dynamo within a partially differentiated CM parent body [e.g., (*137*)]. Thermal modeling indicates that convective core dynamos in mantled planetesimals should be delayed by at least 4 to 5 Ma after accretion (*156*, *157*) due to thermal blanketing of the core by the silicate mantle, which was heated by the decay of the short-lived radionuclide ^{26}Al. However, such a delay need not apply to dynamos powered by other mechanisms like impacts (*158*) or mantle precession (*159*). Assuming that the thermal blanketing constraint is relevant to the CM parent body, the ~2 Ma age of CM chondrite NRM would indicate that they recorded the nebular magnetic field. The CM data therefore suggest that the nebular field in the outer solar system lasted until at least ~2.51 Ma after CAI formation (Fig. 7).

Recent studies of four slightly younger meteorite groups found no evidence of a nebular field (Fig. 7). Paleomagnetic studies of chondrules from two CR chondrites demonstrate that they too pass fusion crust and conglomerate tests (*160*). However, because of the relatively low fidelity of their magnetic recording properties, only an upper bound on the instantaneous field of 0.08 G at 3.68 ± 0.22 Ma after CAI formation at ~3 to 7 AU (*153*) can be placed on the nebular field from CR chondrules. The absence of primary magnetization in the ungrouped achondrite NWA 7325 (*124*) indicates that it cooled in a field of instantaneous intensity of <0.034 G at ~1 to 3 AU (*161*, *162*) at 5.24 ± 0.05 Ma after CAI formation (Fig. 6). Second, the absence of stable high blocking temperature magnetization in the Kaba CV chondrite (*163*) indicates that the time-averaged ambient field was $\lesssim$0.003 G at ~3 to 4 AU (*153*) at 4.08 ± 0.81 Ma after CAI formation. Third, the absence of primary magnetization in three angrites (*164*) indicate that they too cooled in the absence of a nebular field (instantaneous value, <0.006 G) at ~1 to 3 AU (*165*) at a mean age of ~3.71 ± 0.23 Ma after CAI formation.

Spacecraft measurements

Spacecraft have measured the magnetic field at the surface of two asteroids, during flybys of five other asteroids, and at the surface of a comet (*166*–*168*). Although two of the asteroid flybys have tentatively identified remanent magnetic fields, these detections are ambiguous. Moreover, several investigations placed stringent upper limits on the mean asteroid NRM that are at the lower range of the values measured for centimeter-sized samples of meteoritic materials ($<2 \times 10^{-6}$ emu g^{-1}). However, because these missions only constrained the magnetization averaged over spatial scales ranging from 10 to 20 cm [as inferred from recent Hayabusa2 measurements across the surface of asteroid (162173) Ryugu (*167*)] to 10^5 km^3 [as inferred from asteroid (21) Lutetia (*169*)], the intensity of the finer-scale NRM in these asteroids may be well above these limits. Furthermore, with the possible exception of the comet measurements, the timing of the magnetization records in these asteroids is unknown because of the lack of radiometric and other ages for their constituents. Therefore, the paleointensity constraints inferred from meteorites are not inconsistent with lack of detections of remanent magnetic fields around asteroids. An unprecedented opportunity to synthesize magnetic field datasets from spacecraft and laboratory measurements will be provided by returned Hayabusa2 and OSIRIS-REx samples to Earth in the next few years (*170*).

The magnetic field measurements measured by the Rosetta lander Philae at the Jupiter family comet 67P Churyumov-Gerasimenko offer a unique constraint on nebular magnetism. Other than being the only near-field measurements at a comet, the 67P measurements are also distinguished by the fact that they were taken as part of a near-surface >1-km-long transect with four separate landings during which the magnetometer sensor reached within 5 cm of the surface (*168*). Philae constrained the magnetization of the comet to

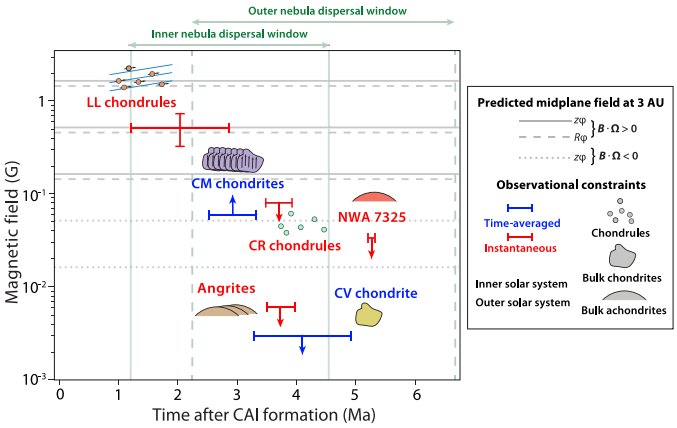

Fig. 7. Paleomagnetic constraints on nebular field as a function of time. Red and blue colors denote the instantaneous (red) and time-averaged (over >1 to 10^6 years) (blue) paleointensities, respectively, from LL (*10*, *155*) and CR chondrules (*160*), bulk samples of CM chondrites (*134*), NWA 7325 (*124*), angrites (*164*), and a CV chondrite (*163*), and spacecraft measurements comet 67P/Churyumov-Gerasimenko (*171*). Downward (upward) arrows indicate upper (lower) limits. Horizontal lines show the predicted midplane field at 3 AU assuming that magnetic stresses are driving accretion around a 1 $M_\odot$ star. Solid and dashed lines denote field assuming that the nebular field and sense of disk rotation are aligned, for which we assume contributions from both $R\phi$ (Eq. 2 with $f = 50$ and L_z~$6H$) and $z\phi$ (dashed) (Eq. 3 with $f' = 10$ and taking $m = 10$) stresses, respectively. Dotted line denotes field assuming that the nebular field and sense of disk rotation are anti-aligned, for which we assume contributions from just $z\phi$ stresses (dashed) (Eq. 3 with $f' = 10$ and taking $m = 1$). For each case, fields are estimated for three assumed different accretion rates: 10^{-9}, 10^{-8}, and 10^{-7} $M_\odot$ year^{-1} (bottom, middle, and top lines). See tables S1 and S2 for source data.

$<5 \times 10^{-6}$ emu g^{-1} for spatial scales of >10 cm (*171*). Other data from Rosetta suggest that 67P accreted by pebble-pile processes, which would indicate the presence of the nebula during its assembly (*172*). In this case, 67P could have acquired ADRM in a sufficiently strong nebular field. Given the evidence that solids in 67P and other Jupiter family comets have chondrite-like compositions and mineralogies (*173*, *174*), assuming such an ADRM has been preserved since the comet formed, the very low NRM intensity would constrain the local nebular field to be <0.03 G (*171*). Given the expected formation locations of Jupiter family comets like 67P, this would apply to somewhere in the region 15 to 45 AU.

DISCUSSION

Support for a central role of magnetism in stellar accretion?

The paleointensity constraints on the nebular field of 0.54 ± 0.21 G at 2.03 ± 0.81 Ma after CAI formation from LL chondrites and of >0.06 G at 2.90 ± 0.39 Ma after CAI formation from CM chondrites are both consistent with the field predicted by Eqs. 3 and 4 for accretion rates of ~10^{-8} $M_\odot$ year^{-1} for a disk whose rotation vector and magnetic field are aligned (see the "Relating paleomagnetic measurements to astrophysical constraints" section) (Fig. 8). The expected field for the case of anti-aligned polarity for this accretion rate would be about an order of magnitude lower (Fig. 8). The anti-aligned polarity would be consistent with the data if the disk accretion rate were on the order of ~10^{-7} $M_\odot$ year^{-1} or higher. This is not impossible if the disk evolution is far from steady state, but otherwise, if the bulk accretion rate is a non-increasing function of time as observations suggest (*7*, *175*), then the mass of the solar nebula would have to be unusually massive, at least reaching a substantial fraction of a solar mass.

Furthermore, the dependence of the field with distance as constrained by the LL chondrules, CM bulk chondrites, and Philae measurements at 67P is broadly consistent with the predicted decrease in field with distance from the Sun (Fig. 8). In particular, the lower limit from CM chondrites, together with the estimated field strength from LL chondrites, is broadly consistent with a temporally constant accretion rate. However, this tentative inference requires more paleomagnetic data for confirmation.

Distinguish between chondrule formation mechanisms?

Nebular paleomagnetic records also constrain how the first solids formed. In particular, chondrules are 0.1- to 1-mm-diameter igneous inclusions found in nearly all primitive, undifferentiated meteorites. Their ubiquity in the meteorite record suggests that they may have constituted a significant fraction of accreted mass in early-forming planetesimals, although this may reflect bias in the formation mechanisms and/or locations of chondrites. The formation mechanism of chondrules remains vigorously debated, with nebular shocks and planetesimal collisions being the subjects of most recent research.

Two observable features of chondrule NRMs can provide information about chondrule formation. First, the existence of primary, unidirectional NRM blocked across a range of temperatures implies that the orientation of the chondrule rotation axis and the background magnetic field remained stable over the time of NRM acquisition, which likely ranged between hours to less than ~10 days (*176*). The presence of such magnetization in Semarkona chondrules has been used to argue for a chondrule number density of less than 4×10^{-2} cm^{-3} during chondrule formation and background PPD temperatures of <230°C, which appears inconsistent with the current sheet and short-circuit instability hypotheses for chondrule formation (*176*, *177*). This result further implies that magnetic fields in the solar nebula during Semarkona chondrule formation were stable over hours to ~10-day time scales.

Second, the paleointensities derived from NRM components can be compared to those predicted for different chondrule formation mechanisms. Among these, the X-wind model posits the Sun as the energy source that led to chondrule melting, while the impact model invokes the energy derived from collisions between planetesimal bodies. Shock waves in the nebular gas, generated at the large scale by GIs or at the local scale by planetary bow shock, have also been hypothesized to lead to chondrule formation. Predictions of strong magnetic fields of ≥0.8 G from the X-wind model of chondrule formation appear inconsistent with values recovered from Semarkona and CM chondrules (*10*). Models of planetesimal impacts and bow shocks suggest that chondrules formed by these processes should record background nebular field intensities, while chondrules formed by large-scale nebular shocks might record a field amplified by a factor of up to 30 above the background (*155*, *177*). This implies that both planetesimal collisions and bow shocks are simultaneously consistent with magnetically mediated nebular transport (see Eqs. 3 and 4) and LL- and CM-derived paleointensities. Meanwhile, large-scale shocks may also be consistent with magnetic transport and the meteorite measurements if the field that magnetized CM meteorites is well significantly above the minimum paleointensities inferred from those meteorites (i.e., well above 0.06 G).

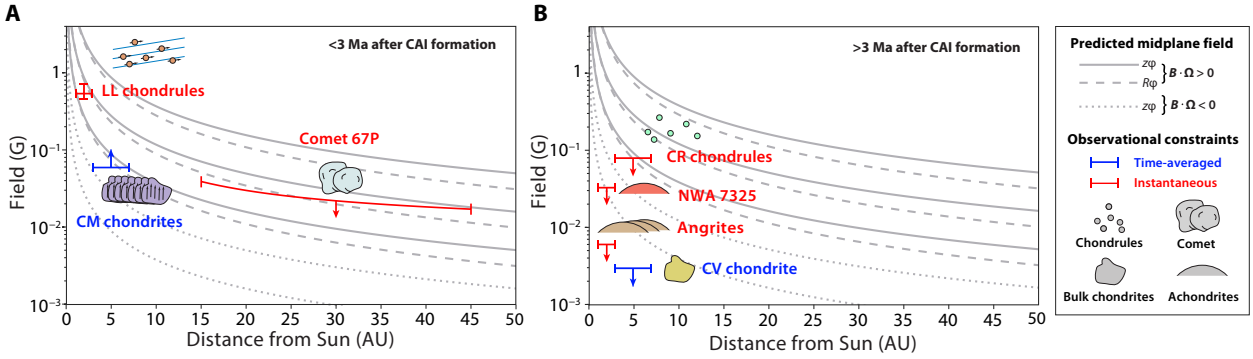

Fig. 8. Paleomagnetic constraints on the nebular field as a function of distance from the young Sun. (**A**) Before 3 Ma after CAI formation. (**B**) After 3 Ma after CAI formation. Red and blue colors indicate instantaneous (red) and time-averaged (over >1 to 10^6 years) (blue) paleointensities, respectively, from LL (*10*, *155*) and CR chondrules (*160*), bulk samples of CM chondrites (*134*), NWA 7325 (*124*), angrites (*164*), and a CV chondrite (*163*), and spacecraft measurements at comet 67P/Churyumov-Gerasimenko (*171*). Downward (upward) arrows indicate upper (lower) limits. Curves show the predicted midplane field assuming that magnetic stresses are driving accretion around a 1 $M_\odot$ star. Solid and dashed curves denote field assuming that the nebular field and sense of disk rotation are aligned, for which we assume contributions from both $R\phi$ (Eq. 2 with $f = 50$ and $L_z \sim 6H$) and $z\phi$ (dashed) (Eq. 3 with $f' = 10$ and taking $m = 10$) stresses, respectively. Dotted curves denote field assuming that the nebular field and sense of disk rotation are anti-aligned, for which we assume contributions from just the $z\phi$ stress (dashed) (Eq. 3 with $f' = 10$ and taking $m = 1$). For each case, fields are estimated for three assumed different accretion rates: 10^{-9}, 10^{-8}, and 10^{-7} $M_\odot$ year^{-1} (bottom, middle, and top curves). See tables S1 and S2 for source data.

Lifetime of the nebula?

Because the sustenance of magnetic fields requires the existence of a conducting medium as a necessary (although not sufficient) condition, the dispersal time of the nebula may be similar to the time when strong magnetic fields like those expected for the nebula (see predictions in Figs. 7 and 8) disappeared as inferred from the absence of paleomagnetism in meteorites younger than a certain age (Figs. 7 and 8 and tables S1 and S2) (*164*). For example, the interplanetary magnetic field at 10 Ma after CAI formation is estimated to have only been ~2 mG at 1 AU (*178*), which is more than an order of magnitude below the weakest nebular fields predicted for an accretion rate of 10^{-9} $M_\odot$ year^{-1}. The minimum lifetime of the nebular field in the inner and outer solar system is constrained by the NRM in LL chondrules and CM bulk chondrites, which have minimum ages of 1.22 and 2.51 Ma after CAI formation, respectively (95% confidence lower limits). These provide a minimum constraint on the lifetime of the nebular field in each location. The most temporally precise constraint on the maximum lifetime of the nebular field comes from the angrites (*164*). Using Eqs. 2 and 3, their <0.006 G paleointensity constraint indicates that by 3.71 ± 0.23 Ma after CAI formation, accretion rates dropped in the inner solar system (<3 AU) to <10^{-12} $M_\odot$ year^{-1} and <10^{-10} $M_\odot$ year^{-1}, assuming that the disk rotation and poloidal fields were aligned and anti-aligned, respectively. We favor the former upper limit because the LL chondrule data support the aligned case for our solar system. These results are broadly consistent with the <0.003 G constraint from the CV chondrite Kaba, which indicates a low accretion rate in the outer solar system (~3 to 7 AU) (*153*, *154*) at 4.08 ± 0.81 Ma after CAI formation. However, because the Kaba paleointensities are recorded by a CRM, this upper limit is uncertain (see above).

The <10^{-12} $M_\odot$ year^{-1} accretion rate inferred from angrites is below the slowest observed accretion rates for PPDs (*179*–*181*). We therefore place a 95% confidence upper limit on the lifetime of the nebula in the inner solar system of 3.94 Ma after CAI formation (*164*) (Fig. 7), calculated as the sum of the weighted U-Pb age for two angrites and the 95% confidence limit on the angrite and CAI U-Pb ages published in the refereed literature combined in quadrature (table S1). Likewise, we estimate a maximum lifetime for the nebula in the outer solar system of 4.89 Ma (Fig. 7), calculated as the sum of the Mn-Cr age for CV chondrules plus the 95% confidence limits on the Mn-Cr ages, the U-Pb age of the D'Orbigny standard and the U-Pb age of CAIs added in quadrature (table S1). Overall, the results indicate that the nebula had locally dispersed sometime between 1.22 and 3.94 Ma after CAI formation in the inner solar system and between 2.51 and 4.89 Ma in the outer solar system, consistent with very recent independent estimates of the lifetime of the nebular gas (*182*) and dust disk (*183*).

This result has implications for how the gas giants Jupiter and Saturn formed. There are two main formation models for giant planets. In the disk instability model, a sufficiently massive disk, subject to the GI and rapid cooling, fragments into clumps within <1000 years, which then cool to become giant planets (*184*). By comparison, core accretion is typically a multistage process beginning with the protracted growth of ~10 to 20 $M_\oplus$ followed by rapid runaway gas accretion that, in total, typically requires $\gtrsim$1 Ma (*184*–*186*). The viability of the core accretion model requires that the disk lifetime must therefore exceed ~1 Ma, consistent with astronomical observations of young stellar objects (*3*). The minimum 1.22-Ma lifetime of the nebula established by paleomagnetic studies therefore permits both the disk instability and core accretion models for gas giant formation in our solar system.

Constraining formation distances of meteorites?

It is conceivable that instead of using paleomagnetic studies to constrain the nebular field intensity, the unknown formation locations of meteorites could be constrained using paleomagnetic measurements if the radial dependence of the field intensity were independently known. In particular, if it is assumed that accretion is being driven by magnetic fields at an accretion rate of ~10^{-8} $M_\odot$ year^{-1}, then the paleointensity measured from a given meteorite or body from an unknown location could potentially constrain the distance from the Sun at which it acquired its magnetic record. In support of this possibility, existing data, although sparse, are broadly consistent with the predicted radial dependence of the nebular fields (Fig. 8). There are numerous uncertainties with such

an approach, beginning with the requirement that magnetic fields be driving accretion and also including assumptions about angular momentum transport (from $\mathcal{T}_{R\phi}$ versus $\mathcal{T}_{z\phi}$), the assumed accretion rate, and the possibility of local field heterogeneities. As implied by the discussion above, the uncertainty on the predicted field as a function of the formation distance from the Sun has an uncertainty of at least an order of magnitude (*81*).

In this context, two recent studies of the ungrouped C2 chondrites Tagish Lake and WIS 91600 measured weak to null paleointensities (<0.0015 and 0.044 ± 0.028 G, respectively) despite the inference that they formed during the lifetime of the solar nebula (i.e., at <3 to 4 Ma after CAI formation). Using the above logic, these studies proposed that these meteorites formed at the current location of Saturn or beyond. This is broadly consistent with predictions from Fig. 8 assuming a minimum accretion rate of 10^{-9} $M_{\odot}$ year^{-1}, the weaker midplane fields predicted for $R\phi$ stresses, and that the disk rotation and poloidal fields were aligned. If correct, this would provide evidence for large-scale radial mass transport sometime during the last few billion years and would support the proposal that these samples may be from comet- or Kuiper belt–like parent bodies.

OUTLOOK AND UNSOLVED QUESTIONS

The study of PPD magnetism is advancing rapidly. From a theoretical standpoint, the recent inclusion of all three diffusivities associated with nonideal MHD effects in the state-of-the-art numerical simulations has fundamentally improved our understanding of the role of magnetic fields in driving angular momentum transport in disks. More work is necessary to extend these studies to three dimensions and to incorporate more realistic physics, especially for thermodynamics and ionization chemistry [e.g., (*187*, *188*)]. Moreover, the current paradigm requires the presence of a net vertical magnetic flux threading the disk, which directly determines the rate of angular momentum transport and the associated field strength. While such magnetic flux is likely inherited from the star formation process, it remains to be understood how it evolves in disks [e.g., (*189*)], which is a more fundamental question relating to the long-term evolution of disks and disk magnetism. As we learn more in the near future, we anticipate that the overall interpretive framework outlined in this review will remain valid, while some of the uncertainties may be narrowed down.

On the observational side, the search for magnetic field signatures in disks continues. While polarized dust continuum emission has thus far been found to be largely of nonmagnetic origin, it still provides useful constraint on disk and dust properties. The marginal detection of the GK effect (*114*) opens up a new approach to potentially constrain the field morphology in disks. Anticipated near-future measurements of the GK effect for more sources and spectral lines will provide valuable information on our understanding of disk magnetic fields. Probably the most promising technique for magnetic studies is the prospect of directly inferring the line-of-sight field strength from measuring the circular polarization signature of CN (and possibly other molecular) lines due to Zeeman splitting from ALMA. Although the extreme sensitivity requirement precludes spatially resolving the field, the information would still allow for directly comparing the field strength with instantaneous accretion rate to validate the theory.

The spatial and time dependence of the nebular field in our own solar system remain poorly understood. These gaps will be addressed with the continued paleomagnetic measurement of new meteorite groups. In particular, just 4 of the ~13 known chondrite groups and just 2 achondrite parent bodies have been studied from the perspective of constraining nebular magnetism. Measurements of a diversity meteorites from different locations in the disk would further constrain the time required for the nebular field to disperse within the inner ~7 AU of the solar system. Furthermore, with regard to chondrites, field records have been obtained from just chondrules and bulk matrix-rich samples. Future analyses of CAIs could provide field records from the beginning of solar system history. Such data could also be used to address the question of how CAIs formed (*190*): Some formation locations (e.g., within <0.1 AU of the young Sun) predict that they would record strong paleointensities, while others (e.g., in the expanding envelope of a supernova) seem to predict near-zero field values.

In this regard, nebular field constraints from spacecraft measurements of small bodies like comet 67P are especially valuable because of the additional constraints on the parent body's formation location provided by the geologic context of in situ measurements. Hence, future sample return missions, like those in progress to carbonaceous asteroids [e.g., (*167*)], are even more exciting, because they will combine the advantage of geologic context with the sensitivity and precision of laboratory measurements.

SUPPLEMENTARY MATERIALS

Supplementary material for this article is available at http://advances.sciencemag.org/cgi/content/full/7/1/eaba5967/DC1

REFERENCES AND NOTES

1. J. P. Williams, L. A. Cieza, Protoplanetary disks and their evolution. *Annu. Rev. Astron. Astrophys.* **49**, 67–117 (2011).
2. Z.-Y. Li, R. Banerjee, R. E. Pudritz, J. K. Jørgensen, H. Shang, R. Krasnopolsky, A. Maury, The earliest stages of star and planet formation: Core collapse, and the formation of disks and outflows, in *Protostars and Planets VI*, H. Beuther, R. S. Klessen, C. P. Dullemond, T. Henning, Eds. (University of Arizona Press, 2014), pp. 173–194.
3. K. E. Haisch Jr., E. A. Lada, C. J. Lada, Disk frequencies and lifetimes in young clusters. *Astrophys. J.* **553**, L153–L156 (2001).
4. A. J. W. Richert, K. V. Getman, E. D. Feigelson, M. A. Kuhn, P. S. Broos, M. S. Povich, M. R. Bate, G. P. Garmire, Circumstellar disc lifetimes in numerous galactic young stellar clusters. *Mon. Not. R. Astr. Soc.* **477**, 5191–5206 (2018).
5. S. M. Andrews, J. Huang, L. M. Pérez, A. Isella, C. P. Dullemond, N. T. Kurtovic, V. V. Guzmán, J. M. Carpenter, D. J. Wilner, S. Zhang, Z. Zhu, T. Birnstiel, X.-N. Bai, M. Benisty, A. M. Hughes, K. I. Öberg, L. Ricci, The disk substructures at high angular resolution project (DSHARP). I. Motivation, sample, calibration, and overview. *Astrophys. J. Lett.* **869**, L41 (2018).
6. F. Long, P. Pinilla, G. J. Herczeg, D. Harsono, G. Dipierro, I. Pascucci, N. Hendler, M. Tazzari, E. Ragusa, C. Salyk, S. Edwards, G. Lodato, G. van de Plas, D. Johnstone, Y. Liu, Y. Boehler, S. Cabrit, C. F. Manara, F. Menard, G. D. Mulders, B. Nisini, W. J. Fischer, E. Rigliaco, A. Banzatti, H. Avenhaus, M. Gully-Santiago, Gaps and rings in an ALMA survey of disks in the Taurus star-forming region. *Astrophys. J.* **869**, 17 (2018).
7. L. Hartmann, N. Calvet, E. Gullbring, P. D'Alessio, Accretion and the evolution of T Tauri disks. *Astrophys. J.* **495**, 385–400 (1998).
8. R. Alexander, I. Pascucci, S. Andrews, P. Armitage, L. Cieza, The dispersal of protoplanetary disks, in *Protostars and Planets VI*, H. Beuther, R. S. Klessen, C. P. Dullemond, T. Henning, Eds. (University of Arizona Press, 2014), pp. 475–496.
9. C. L. H. Hull, H. Yang, Z.-Y. Li, A. Kataoka, I. W. Stephens, S. Andrews, X. Bai, L. I. Cleeves, A. M. Hughes, L. Looney, L. M. Pérez, D. Wilner, ALMA observations of polarization from dust scattering in the IM Lup protoplanetary disk. *Astrophys. J.* **860**, 82 (2018).
10. R. R. Fu, B. P. Weiss, E. A. Lima, R. J. Harrison, X.-N. Bai, S. J. Desch, D. S. Ebel, C. Suavet, H. Wang, D. Glenn, D. L. Sage, T. Kasama, R. L. Walsworth, A. T. Kuan, Solar nebula magnetic fields recorded in the Semarkona meteorite. *Science* **346**, 1089–1092 (2014).
11. X.-N. Bai, Toward a global evolutionary model of protoplanetary disks. *Astrophys. J.* **821**, 80 (2016).
12. N. I. Shakura, R. A. Sunyaev, Black holes in binary systems. Observational appearance. *Astron. Astrophys.* **24**, 337–355 (1973).
13. C. Hayashi, Structure of the solar nebula, growth and decay of magnetic fields and effects of magnetic and turbulent viscosities on the nebula. *Prog. Theoret. Phys. Suppl.* **70**, 35–53 (1981).

14. S. Fromang, G. Lesur, Angular momentum transport in accretion disks: A hydrodynamical perspective. *EAS Publ. Series* **82**, 391–413 (2019).
15. W. Lyra, O. M. Umurhan, The initial conditions for planet formation: Turbulence driven by hydrodynamical instabilities in disks around young stars. *Publ. Astron. Soc. Pac.* **141**, 072001 (2019).
16. L. Rayleigh, On the dynamics of revolving fluids. *Proc. R. Soc. London A.* **93**, 148–154 (1917).
17. S. A. Balbus, Magnetohydrodynamics of protostellar disks, in *Physical Processes in Circumstellar Disks Around Young Stars*, P. J. V. Garcia, Ed. (University of Chicago Press, 2011), pp. 237–282.
18. S. Grossmann, The onset of shear flow turbulence. *Rev. Mod. Phys.* **72**, 603–618 (2000).
19. S. Grossmann, D. Lohse, C. Sun, High–Reynolds number Taylor-Couette turbulence. *Annu. Rev. Fluid Mech.* **48**, 53–80 (2016).
20. G. Lesur, P.-Y. Longaretti, On the relevance of subcritical hydrodynamic turbulence to accretion disk transport. *Astron. Astrophys.* **444**, 25–44 (2005).
21. J.-L. Tassoul, *Theory of Rotating Stars* (Princeton Univ. Press, 1978), p. 524.
22. M.-K. Lin, A. N. Youdin, Cooling requiremens for the vertical shear instability in protoplanetary disks. *Astrophys. J.* **811**, 17 (2015).
23. R. P. Nelson, O. Gressel, O. M. Umurhan, Linear and non-linear evolution of the vertical shear instability in accretion discs. *Mon. Not. R. Astron. Soc.* **435**, 2610–2632 (2013).
24. M. H. R. Stoll, W. Kley, Particle dynamics in discs with turbulence generated by the vertical shear instability. *Astron. Astrophys.* **594**, A57 (2016).
25. H. Klahr, A. Hubbard, Convective overstability in radially stratified accretion disks under thermal relaxation. *Astrophys. J.* **788**, 21 (2014).
26. W. Lyra, Convective overstability in accretion disks: Three-dimensional linear analysis and nonlinear saturation. *Astrophys. J.* **789**, 77 (2014).
27. H. N. Latter, On the convective overstability in protoplanetary discs. *Mon. Not. R. Astr. Soc.* **455**, 2608–2618 (2016).
28. H. H. Klahr, P. Bodenheimer, Turbulence in accretion disks: Vorticity generation and angular momentum transport via the global baroclinic instability. *Astrophys. J.* **582**, 869–892 (2003).
29. G. Lesur, J. C. B. Papaloizou, The subcritical baroclinic instability in local accretion disc models. *Astron. Astrophys.* **513**, A60 (2010).
30. N. Raetting, W. Lyra, H. Klahr, A parameter study for baroclinic vortex amplification. *Astrophys. J.* **765**, 115 (2013).
31. P. S. Marcus, S. Pei, C.-H. Jiang, P. Hassanzadeh, Three-dimensional vortices generated by self-replication in stably stratified rotating shear flows. *Phys. Rev. Lett.* **111**, 084501 (2013).
32. O. M. Umurhan, K. Sharif, J. N. Cuzzi, Critical layers and protoplanetary disk turbulence. *Astrophys. J.* **830**, 95 (2016).
33. G. R. J. Lesur, H. N. Latter, On the survival of zombie vortices in protoplanetary discs. *Mon. Not. R. Astr. Soc.* **462**, 4549–4554 (2016).
34. P. S. Marcus, S. Pei, C.-H. Jiang, J. A. Barranco, P. Hassanzadeh, D. Lecoanet, Zombie vortex instability. I. A purely hydrodynamic instability to resurrect the dead zones of protoplanetary disks. *Astrophys. J.* **808**, 87 (2015).
35. K. Kratter, G. Lodato, Gravitational instabilities in circumstellar disks. *Annu. Rev. Astron. Astrophys.* **54**, 271–311 (2016).
36. A. Toomre, On the gravitational stability of a disk of stars. *Astrophys. J.* **139**, 1217–1238 (1964).
37. C. F. Gammie, Nonlinear outcome of gravitational instability in cooling, gaseous disks. *Astrophys. J.* **553**, 174–183 (2001).
38. K. Tomida, M. N. Machida, T. Hosokawa, Y. Sakurai, C. H. Lin, Grand-design spiral arms in a young forming circumstellar disk. *Astrophys. J. Lett.* **835**, L11 (2017).
39. C.-F. Lee, Z.-Y. Li, N. J. Turner, Spiral structures in an embedded protostellar disk driven by envelope accretion. *Nat. Astron.* **4**, 142–146 (2020).
40. Z. Zhu, R. Dong, J. M. Stone, R. R. Rafikov, The structure of spiral shocks excited by planetary-mass companions. *Astrophys. J.* **813**, 88 (2015).
41. R. R. Rafikov, Protoplanetary disk heating and evolution driven by spiral density waves. *Astrophys. J.* **831**, 122 (2016).
42. R. V. E. Lovelace, H. Li, S. A. Colgate, A. F. Nelson, Rossby wave instability of Keplerian accretion disks. *Astrophys. J.* **513**, 805–810 (1999).
43. H. Li, S. A. Colgate, B. Wendroff, R. Liska, Rossby wave instability of thin accretion disks. III. Nonlinear simulations. *Astrophys. J.* **551**, 874–896 (2001).
44. H. Meheut, F. Casse, P. Varniere, M. Tagger, Rossby wave instability and three-dimensional vortices in accretion disks. *Astron. Astrophys.* **516**, A31 (2010).
45. H. Alfvén, *On the Origin of the Solar System* (Oxford Univ. Press, 1954), 194 p.
46. M. Wardle, Magnetic fields in protoplanetary disks. *Astrophys. Space Sci.* **311**, 35–45 (2007).
47. X.-N. Bai, J. Goodman, Heat and dust in active layers of protostellar disks. *Astrophys. J.* **701**, 737–755 (2009).
48. P. J. Armitage, Physical processes in protoplanetary disks, in *From Protoplanetary Disks to Planet Formation*, M. Audard, M. R. Meyer, Y. Alibert, Eds. (Springer, 2015), pp. 1–150.
49. S. A. Balbus, J. F. Hawley, A powerful local shear instability in weakly magnetized disks. I. Linear analysis. *Astrophys. J.* **376**, 214–233 (1991).
50. R. D. Blandford, D. G. Payne, Hydromagnetic flows from accretion disks and the production of radio jets. *Mon. Not. R. Astr. Soc.* **199**, 883–903 (1982).
51. R. M. Kulsrud, *Plasma Physics for Astrophysics* (Princeton Univ. Press, 2005).
52. J. F. Hawley, C. F. Gammie, S. A. Balbus, Local three-dimensional magnetohydrodynamic simulations of accretion disks. *Astrophys. J.* **440**, 742–763 (1995).
53. S. W. Davis, J. M. Stone, M. E. Pessah, Sustained magnetorotational turbulence in local simulations of stratified disks with zero net magnetic flux. *Astrophys. J.* **713**, 52–65 (2010).
54. X.-N. Bai, J. M. Stone, Local study of accretion disks with a strong vertical magnetic field: Magnetorotational instability and disk outflow. *Astrophys. J.* **767**, 30 (2013).
55. R. M. Crutcher, Magnetic fields in molecular clouds. *Annu. Rev. Astron. Astrophys.* **50**, 29–63 (2012).
56. S. J. Desch, N. J. Turner, High-temperature ionization in protoplanetary disks. *Astrophys. J.* **811**, 156 (2015).
57. T. Umebayashi, T. Nakano, Fluxes of energetic particles and the ionization rate in very dense interstellar clouds. *Publ. Astron. Soc. Japan* **33**, 617–635 (1981).
58. J. Igea, A. E. Glassgold, X-ray ionization of the disks of young stellar objects. *Astrophys. J.* **518**, 848–858 (1999).
59. D. Perez-Becker, E. Chiang, Surface layer accretion in conventional and transitional disks driven by far-ultraviolet ionization. *Astrophys. J.* **735**, 8 (2011).
60. X.-N. Bai, Magnetorotational-instability-driven accretion in protoplanetary disks. *Astrophys. J.* **739**, 50 (2011).
61. N. J. Turner, T. Sano, N. Dziourkevitch, Turbulent mixing and the dead zone in protostellar disks. *Astrophys. J.* **659**, 729–737 (2007).
62. C. F. Gammie, Layered accretion in T Tauri disks. *Astrophys. J.* **457**, 355–362 (1996).
63. T. Fleming, J. M. Stone, Local magnetohydrodynamic models of layered accretion disks. *Astrophys. J.* **585**, 908–920 (2003).
64. X.-N. Bai, J. M. Stone, Effect of ambipolar diffusion on the nonlinear evolution of magnetorotational instability in weakly ionized disks. *Astrophys. J.* **736**, 144 (2011).
65. X.-N. Bai, J. M. Stone, Wind-driven accretion in protoplanetary disks. I. Suppression of the magnetorotational instability and launching of the magnetocentrifugal wind. *Astrophys. J.* **769**, 76 (2013).
66. O. Gressel, N. J. Turner, R. P. Nelson, C. P. McNally, Global simulations of protoplanetary disks with ohmic resistivity and ambipolar diffusion. *Astrophys. J.* **801**, 84 (2015).
67. J. B. Simon, X.-N. Bai, P. J. Armitage, J. M. Stone, K. Beckwith, Turbulence in the outer regions of protoplanetary disks. II. Strong accretion driven by a vertical magnetic field. *Astrophys. J.* **775**, 73 (2013).
68. J. B. Simon, X.-N. Bai, K. M. Flaherty, A. M. Hughes, Origin of weak turbulence in the outer regions of protoplanetary disks. *Astrophys. J.* **865**, 10 (2018).
69. D. Gubbins, K. Zhang, Symmetry properties of the dynamo equations for palaeomagnetism and geomagnetism. *Phys. Earth Planet. Inter.* **75**, 225–241 (1993).
70. X.-N. Bai, Hall-effect-controlled gas dynamics in protoplanetary disks. I. Wind solutions at the inner disks. *Astrophys. J.* **791**, 137 (2014).
71. G. Lesur, M. W. Kunz, S. Fromang, Thanatology in protoplanetary discs: The combined influence of Ohmic, Hall, and ambipolar diffusion on dead zones. *Astron. Astrophys.* **566**, A56 (2014).
72. M. W. Kunz, On the linear stability of weakly ionized, magnetized planar shear flows. *Mon. Not. R. Astr. Soc.* **385**, 1494–1510 (2008).
73. X.-N. Bai, Hall effect controlled gas dynamics in protoplanetary disks. II. Full 3D simulations toward the outer disk. *Astrophys. J.* **798**, 84 (2015).
74. T. Sano, J. M. Stone, The effect of the Hall term on the nonlinear evolution of the magnetorotational instability. II. Saturation level and critical magnetic Reynolds number. *Astrophys. J.* **577**, 534–553 (2002).
75. M. W. Kunz, G. Lesur, Magnetic self-organization in Hall-dominated magnetorotational turbulence. *Mon. Not. R. Astr. Soc.* **434**, 2295–2312 (2013).
76. J. B. Simon, G. Lesur, M. W. Kunz, P. J. Armitage, Magnetically driven accretion in protoplanetary discs. *Mon. Not. R. Astr. Soc.* **454**, 1117–1131 (2015).
77. T. Tsukamoto, K. Iwasaki, S. Okuzumi, M. N. Machida, S. Inutsuka, Bimodality of circumstellar disk evolution induced by the Hall current. *Astrophys. J. Lett.* **810**, L26 (2015).
78. J. Wurster, D. J. Price, M. R. Bate, Can non-ideal magnetohydrodynamics solve the magnetic braking catastrophe? *Mon. Not. R. Astr. Soc.* **457**, 1037–1061 (2016).
79. X.-N. Bai, Global simulations of the inner regions of protoplanetary disks with comprehensive disk microphysics. *Astrophys. J.* **845**, 75 (2017).
80. W. Béthune, G. Lesur, J. Ferreira, Global simulations of protoplanetary disks with net magnetic flux: I. Non-ideal MHD case. *Astron. Astrophys.* **600**, A75 (2017).
81. A. Riols, G. Lesur, Spontaneous ring formation in wind-emitting accretion discs. *Astron. Astrophys.* **625**, A108 (2019).
82. X. Hu, Z. Zhu, S. Okuzumi, X.-N. Bai, L. Wang, K. Tomida, J. M. Stone, Nonideal MHD simulation of HL Tau disk: Formation of rings. *Astrophys. J.* **885**, 36 (2019).

83. R. R. Fu, E. A. Lima, B. P. Weiss, R. J. Harrison, D. S. Ebel, S. J. Desch, Nebular magnetism recorded in the Semarkona meteorite. *Lunar Planet Sci. Conf. XLV* , 1420 (2014).
84. M. Audard, P. Ábrahám, M. M. Dunham, J. D. Green, N. Grosso, K. Hamaguchi, J. H. Kastner, A. Kóspál, G. Lodato, M. M. Romanova, S. L. Skinner, E. I. Vorobyov, Z. Zhu, Episodic accretion in young stars, in *Protostars and Planets VI*, H. Beuther, R. S. Klessen, C. P. Dullemond, T. Henning, Eds. (University of Arizona Press, 2014), pp. 387–410.
85. B. T. Draine, Astrophysics of dust in cold clouds, in *The Cold Universe*, D. Pfenninger, Y. Revaz, Eds. (Springer, 2004), pp. 213–304.
86. A. Lazarian, Tracing magnetic fields with aligned grains. *J. Quant. Spectrosc. Radiat. Transfer* **106**, 225–256 (2007).
87. H.-B. Li, C. D. Dowell, A. Goodman, R. Hildebrand, G. Novak, Anchoring magnetic field in turbulent molecular clouds. *Astrophys. J.* **704**, 891–897 (2009).
88. C. L. H. Hull, R. L. Plambeck, W. Kwon, G. C. Bower, J. M. Carpenter, R. M. Crutcher, J. D. Fiege, E. Franzmann, N. S. Hakobian, C. Heiles, M. Houde, A. M. Hughes, J. W. Lamb, L. W. Looney, D. P. Marrone, B. C. Matthews, T. Pillai, M. W. Pound, N. Rahman, G. Sandell, I. W. Stephens, J. J. Tobin, J. E. Vaillancourt, N. H. Volgenau, M. C. H. Wright, TADPOL: A 1.3 mm survey of dust polarization in star-forming cores and regions. *Astrophys. J. Suppl. Ser.* **213**, 13 (2014).
89. Planck Collaboration, Planck intermediate results. XXXII. The relative orientation between the magnetic field and structures traced by interstellar dust. *Astron. Astrophys.* **586**, A135 (2016).
90. A. M. Hughes, D. J. Wilner, J. Cho, D. P. Marrone, A. Lazarian, S. M. Andrews, R. Rao, Stringent limits on the polarized submillimeter emission from protoplanetary disks. *Astrophys. J.* **704**, 1204–1217 (2009).
91. A. M. Hughes, C. L. H. Hull, D. J. Wilner, R. L. Plambeck, Interferometric upper limits on millimeter polarization of the disks around DG Tau, GM Aur, and MWC 480. *Astronom. J.* **145**, 115 (2013).
92. R. Rao, J. M. Girart, S.-P. Lai, D. P. Marrone, Detection of a magnetized disk around a very young protostar. *Astrophys. J.* **780**, L6 (2014).
93. I. W. Stephens, L. W. Looney, W. Kwon, M. Fernández-López, A. M. Hughes, L. G. Mundy, R. M. Crutcher, Z.-Y. Li, R. Rao, Spatially resolved magnetic field structure in the disk of a T Tauri star. *Nature* **514**, 597–599 (2014).
94. D. Li, E. Pantin, C. M. Telesco, H. Zhang, C. M. Wright, P. J. Barnes, C. Packham, N. Mariñas, An ordered magnetic field in the protoplanetary disk of AB Aur revealed by mid-infrared polarimetry. *Astrophys. J.* **832**, 18 (2016).
95. J. Cho, A. Lazarian, Grain alignment and polarized emission from magnetized T Tauri disks. *Astrophys. J.* **669**, 1085–1097 (2007).
96. R. Tazaki, A. Lazarian, H. Nomura, Radiative grain alignment in protoplanetary disks: Implications for polarimetric observations. *Astrophys. J.* **839**, 56 (2017).
97. A. Kataoka, T. Muto, M. Momose, T. Tsukagoshi, M. Fukagawa, H. Shibai, T. Hanawa, K. Murakawa, C. P. Dullemond, Millimeter-wave polarization of protoplanetary disks due to dust scattering. *Astrophys. J.* **809**, 78 (2015).
98. H. Yang, Z.-Y. Li, L. Looney, I. Stephens, Inclination-induced polarization of scattered millimetre radiation from protoplanetary discs: The case of HL Tau. *Mon. Not. R. Astr. Soc.* **456**, 2794–2805 (2016).
99. A. Kataoka, T. Tsukagoshi, M. Momose, H. Nagai, T. Muto, C. P. Dullemond, A. Pohl, M. Fukagawa, H. Shibai, T. Hanawa, K. Murakawa, Submillimeter polarization observation of the protoplanetary disk around HD 142527. *Astrophys. J. Lett.* **831**, L12 (2016).
100. A. Kataoka, T. Tsukagoshi, A. Pohl, T. Muto, H. Nagai, I. W. Stephens, K. Tomisaka, M. Momose, The evidence of radio polarization induced by the radiative grain alignment and self-scattering of dust grains in a protoplanetary disk. *Astrophys. J.* **844**, L5 (2017).
101. I. W. Stephens, H. Yang, Z.-Y. Li, L. W. Looney, A. Kataoka, W. Kwon, M. Fernández-López, C. L. H. Hull, M. Hughes, D. Segura-Cox, L. Mundy, R. Crutcher, R. Rao, ALMA reveals transition of polarization pattern with wavelength in HL Tau's disk. *Astrophys. J.* **851**, 55 (2017).
102. R. E. Harrison, L. W. Looney, I. W. Stephens, Z.-Y. Li, H. Yang, A. Kataoka, R. J. Harris, W. Kwon, T. Muto, M. Momose, Dust polarization in four protoplanetary disks at 3 mm: Further evidence of multiple origins. *Astrophys. J. Lett.* **877**, L2 (2019).
103. A. Kataoka, S. Okuzumi, R. Tazaki, Millimeter-wave polarization due to grain alignment by the gas flow in protoplanetary disks. *Astrophys. J. Lett.* **874**, L6 (2019).
104. H. Yang, Z.-Y. Li, I. W. Stephens, A. Kataoka, L. Looney, Does HL Tau disc polarization in ALMA band 3 come from radiatively aligned grains? *Mon. Not. R. Astr. Soc.* **483**, 2371–2381 (2019).
105. C.-F. Lee, Z.-Y. Li, T.-C. Ching, S.-P. Lai, H. Yang, ALMA dust polarization observations of two young edge-on protostellar disks. *Astrophys. J.* **854**, 56 (2018).
106. P. Cazzoletti, E. F. van Dischoeck, R. Visser, S. Facchini, S. Bruderer, CN rings in full protoplanetary disks around young stars as probes of disk structure. *Astron. Astrophys.* **609**, A93 (2018).
107. R. Brauer, S. Wolf, M. Flock, Magnetic fields in circumstellar disks. The potential of Zeeman observations. *Astron. Astrophys.* **607**, A104 (2017).
108. W. H. T. Vlemmings, B. Lankhaar, P. Cazzoletti, C. Ceccobello, D. Dall'Olio, E. F. van Dishoeck, S. Facchini, E. M. L. Humphreys, M. V. Persson, L. Testi, J. P. Williams, Stringent limits on the magnetic field strength in the disc of TW Hya: ALMA observations of CN polarisation. *Astron. Astrophys.* **624**, L7 (2019).
109. P. Goldreich, N. D. Kylafis, On mapping the magnetic field direction in molecular clouds by polarization measurements. *Astrophys. J.* **243**, L75–L78 (1981).
110. J. Glenn, C. K. Walker, J. H. Bieging, P. R. Jewell, Millimeter-wave spectropolarimetry of evolved stars: Evidence for polarized molecular line emission. *Astrophys. J.* **487**, L89–L92 (1997).
111. J. S. Greaves, W. S. Holland, P. Friberg, W. R. F. Dent, Polarized CO emiission from molecular clouds. *Astrophys. J.* **512**, L139–L142 (1999).
112. J. M. Girart, R. M. Crutcher, R. Rao, Detection of polarized CO emission from the molecular outflow in NGC 1333 IRAS 4A. *Astrophys. J.* **525**, L109–L112 (1999).
113. B. Lankhaar, W. Vlemmings, PORTAL: Three-dimensional polarized (sub)millimeter line radiative transfe. *Astron. Astrophys.* **636**, A14 (2020).
114. I. W. Stephens, M. Fernández-López, Z.-Y. Li, L. W. Looney, R. Teague, Low level carbon monoxide line polarization in two protoplanetary disks: HD 142527 and IM Lup. *Astrophys. J.* **901**, 71 (2020).
115. S.-C. L. L. Lappe, N. S. Church, T. Kasama, A. B. da Silva Fanta, G. Bromiley, R. E. Dunin-Borkowski, J. M. Feinberg, S. Russell, R. J. Harrison, Mineral magnetism of dusty olivine: A credible recorder of preaccretionary remanence. *Geochem. Geophys. Geosyst.* **12**, Q12Z35 (2011).
116. L. Tauxe, S. K. Banerjee, R. F. Butler, V. R. van der, *Essentials of Paleomagnetism: Fifth Web Edition* (Scripps Institution of Oceanography, 2018).
117. J. Gattacceca, L. Berthe, M. Boustie, F. Vadeboin, P. Rochette, T. De Resseguier, On the efficiency of shock magnetization processes. *Phys. Earth Planet. Inter.* **166**, 1–10 (2008).
118. R. R. Fu, B. P. Weiss, Detrital remanent magnetization in the solar nebula. *J. Geophys. Res.* **117**, E02003 (2012).
119. S.-C. L. L. Lappe, J. M. Feinberg, A. R. Muxworthy, R. J. Harrison, Comparison and calibration of nonheating paleointensity methods: A case study using dusty olivine. *Geochem. Geophys. Geosyst.* **14**, 2143–2158 (2013).
120. B. P. Weiss, S. M. Tikoo, The lunar dynamo. *Science* **346**, 1246753 (2014).
121. Y. Yu, Paleointensity determination using anhysteretic remanence and saturation isothermal remanence. *Geochem. Geophys. Geosyst.* **11**, Q02Z12 (2010).
122. J. Gattacceca, P. Rochette, Toward a robust normalized magnetic paleointensity method applied to meteorites. *Earth Planet. Sci. Lett.* **227**, 377–393 (2004).
123. U. Draeger, M. Prévot, T. Poidras, J. Riisager, Single-domain chemical, thermochemical and thermal remanences in a basaltic rock. *Geophys. J. Int.* **166**, 12–32 (2006).
124. B. P. Weiss, H. Wang, T. G. Sharp, J. Gattacceca, D. L. Shuster, B. Downey, J. Hu, R. R. Fu, A. T. Kuan, C. Suavet, A. J. Irving, J. Wang, J. Wang, A nonmagnetic differentiated early planetary body. *Earth Planet. Sci. Lett.* **468**, 119–132 (2017).
125. B. P. Weiss, J. Gattacceca, S. Stanley, P. Rochette, U. R. Christensen, Paleomagnetic records of meteorites and early planetesimal differentiation. *Space Sci. Rev.* **152**, 341–390 (2010).
126. P. Rochette, J. Gattacceca, M. Bourot-Denise, G. Consolmagno, L. Folco, T. Kohout, L. Pesonen, L. Sagnotti, Magnetic classification of stony meteorites: 3. Achondrites. *Meteorit. Planet. Sci.* **44**, 405–427 (2009).
127. A. R. Muxworthy, W. Williams, Critical single-domain grain sizes in elongated iron particles: Implications for meteoritic and lunar magnetism. *Geophys. J. Int.* **202**, 578–583 (2015).
128. L. Nagy, W. Williams, L. Tauxe, A. R. Muxworthy, I. Ferreira, Thermomagnetic recording fidelity of nanometer-sized iron and implications for planetary magnetism. *Proc. Natl. Acad. Sci. U.S.A.* **116**, 1984–1991 (2019).
129. J. F. Einsle, R. J. Harrison, T. Kasama, P. Ó. Conbhuí, K. Fabian, W. Williams, L. Woodland, R. R. Fu, B. P. Weiss, P. A. Midgley, Multi-scale three-dimensional characterization of iron particles in dusty olivine: Implications for paleomagnetism of chondritic meteorites. *Am. Mineral.* **101**, 2070–2084 (2016).
130. J. Shah, W. Williams, T. P. Almeida, L. Nagy, A. R. Muxworthy, A. Kovács, M. A. Valdez-Grijalva, K. Fabian, S. S. Russell, M. J. Genge, R. E. Dunin-Borkowski, The oldest magnetic record in our solar system identified using nanometric imaging and numerical modeling. *Nat. Commun.* **9**, 1173 (2018).
131. C. I. O. Nichols, J. F. Einsle, M.-Y. Im, T. Kasama, Z. Saghi, P. A. Midgley, R. J. Harrison, Field response of magnetic vortices in dusty olivine from the Semarkona chondrite. *Geochem. Geophys. Geosyst.* **20**, 1441–1453 (2019).
132. M. Uehara, J. Gattacceca, H. Leroux, D. Jacob, C. J. van der Beek, Magnetic microstructures of metal grains in equilibrated ordinary chondrites and implications for paleomagnetism of meteorites. *Earth Planet. Sci. Lett.* **306**, 241–252 (2011).
133. J. Gattacceca, C. Suavet, P. Rochette, B. P. Weiss, M. Winklhofer, M. Uehara, J. M. Friedrich, Metal phases in ordinary chondrites: Magnetic hysteresis properties and implications for thermal history. *Meteorit. Planet. Sci.* **49**, 652–676 (2014).
134. C. Cournède, J. Gattacceca, M. Gounelle, P. Rochette, B. P. Weiss, B. Zanda, An early solar system magnetic field recorded in CM chondrites. *Earth Planet. Sci. Lett.* **410**, 62–74 (2015).
135. M. Uehara, J. Gattacceca, P. Rochette, F. Demory, E. M. Valenzuela, Magnetic study of meteorites recovered in the Atacama desert (Chile): Implications for meteorite paleomagnetism and the stability of hot desert surfaces. *Phys. Earth Planet. Inter.* **200-201**, 113–123 (2012).

136. A. N. Krot, M. I. Petaev, E. R. D. Scott, B.-G. Choi, M. E. Zolensky, K. Keil, Progressive alteration in CV3 chondrites: More evidence for asteroidal alteration. *Meteorit. Planet. Sci.* **33**, 1065–1085 (1998).
137. B. P. Weiss, L. T. Elkins-Tanton, Differentiated planetesimals and the parent bodies of chondrites. *Annu. Rev. Earth Planet. Sci.* **41**, 529–560 (2013).
138. B. P. Weiss, J. S. Berdahl, L. Elkins-Tanton, S. Stanley, E. A. Lima, L. Carporzen, Magnetism on the angrite parent body and the early differentiation of planetesimals. *Science* **322**, 713–716 (2008).
139. J. F. Lovering, The magnetic field in a primary meteorite body. *Am. J. Sci.* **257**, 271–275 (1959).
140. F. J. Ciesla, The distributions and ages of refractory objects in the solar nebula. *Icarus* **208**, 455–467 (2010).
141. H. Y. McSween Jr., G. R. Huss, *Cosmochemistry* (Cambridge Univ. Press, 2010), pp. 549.
142. J. N. Connelly, M. Bizzarro, A. N. Krot, Å. Nordlund, D. Wielandt, M. A. Ivanova, The absolute chronology and thermal processing of solids in the solar protoplanetary disk. *Science* **338**, 651–655 (2012).
143. A. Bouvier, G. A. Brennecka, M. Wadhwa, Absolute chronology of the first solids in the solar system, in *Workshop on Formation of the First Solids in the Solar System*, abstract 9054 (2011).
144. M. Miyamoto, T. Mikouchi, R. H. Jones, Cooling rates of porphyritic olivine chondrules in the Semarkona (LL3.00) ordinary chondrite: A model for diffusional equilibration of olivine during fractional crystallization. *Meteorit. Planet. Sci.* **44**, 521–530 (2009).
145. M. Humayun, Chondrule cooling rates inferred from diffusive profiles in metal lumps from the Acfer 097 CR2 chondrite. *Meteorit. Planet. Sci.* **47**, 1191–1208 (2012).
146. M. J. Wick, R. H. Jones, Formation conditions of plagioclase-bearing type I chondrules in CO chondrites: A study of natural samples and experimental analogs. *Geochim. Cosmochim. Acta* **98**, 140–159 (2012).
147. L. Wilson, K. Keil, L. B. Browning, A. N. Krot, W. Bourcier, Early aqueous alteration, explosive disruption, and reprocessing of asteroids. *Meteorit. Planet. Sci.* **34**, 541–557 (1999).
148. P. M. Doyle, K. Jogo, K. Nagashima, A. N. Krot, S. Wakita, F. J. Ciesla, I. D. Hutcheon, Early aqueous activity on the ordinary and carbonaceous chondrite parent bodies recorded by fayalite. *Nat. Commun.* **6**, 7444 (2015).
149. C. P. Dullemond, C. Dominik, Dust coagulation in protoplanetary disks: A rapid depletion of small grains. *Astron. Astrophys.* **434**, 971–986 (2005).
150. L. Testi, T. Birnstiel, L. Ricci, S. Andrews, J. Blum, J. Carpenter, C. Dominik, A. Isella, A. Natta, J. P. Williams, D. J. Wilner, Dust Evolution in Protoplanetary Disks, in *Protostars and Planets VI*, T. Henning, R. Klessen, H. Beuther, C. P. Dullemond, Eds. (University of Arizona Press, 2014), pp. 339–362.
151. M. Gravnik, P. Brown, Identification of meteorite source regions in the Solar System. *Icarus* **311**, 271–287 (2018).
152. T. S. Kruijer, C. Burkhardt, G. Budde, T. Klein, Age of Jupiter inferred from the distinct genetics and formation times of meteorites. *Proc. Natl. Acad. Sci. U.S.A.* **114**, 6712–6716 (2017).
153. S. J. Desch, A. Kalyaan, C. M. O.'. D. Alexander, The effect of Jupiter's formation on the distribution of refractory elements and inclusions in meteorites. *Astrophys. J. Suppl. Ser.* **238**, 11 (2018).
154. S. Sutton, C. M. O'D Alexander, A. Bryant, A. Lanzirotti, M. Newville, E. A. Cloutis, The bulk valence state of Fe and the origin of water in chondrites. *Geochim. Cosmochim. Acta* **211**, 115–132 (2017).
155. C. Mai, S. J. Desch, A. C. Boley, B. P. Weiss, Magnetic fields recorded by chondrules formed in nebular shocks. *Astrophys. J.* **857**, 96 (2018).
156. M. G. Sterenborg, J. W. Crowley, Thermal evolution of early solar system planetesimals and the possibility of sustained dynamos. *Phys. Earth Planet. Inter.* **214**, 53–73 (2013).
157. J. F. J. Bryson, J. A. Neufeld, F. Nimmo, Constraints on asteroid magnetic field evolution and the radii of meteorite parent bodies from thermal modelling. *Earth Planet. Sci. Lett.* **521**, 68–78 (2019).
158. M. Le Bars, M. A. Wieczorek, Ö. Karatekin, D. Cébron, M. Laneuville, An impact-driven dynamo for the early Moon. *Nature* **479**, 215–218 (2011).
159. C. A. Dwyer, D. J. Stevenson, F. Nimmo, A long-lived lunar dynamo driven by continuous mechanical stirring. *Nature* **479**, 212–214 (2011).
160. R. R. Fu, P. Kehayias, B. P. Weiss, D. L. Schrader, X.-N. Bai, J. B. Simon, Weak magnetic fields in the outer solar nebular recorded in CR chondrites. *J. Geophys. Res.* **125**, e2019JE006260 (2020).
161. C. A. Goodrich, N. T. Kita, Q.-Z. Yin, M. E. Sanborn, C. D. Williams, D. Nakashima, M. D. Lane, S. Boyle, Petrogenesis and provenance of ungrouped achondrite Northwest Africa 7325 from petrology, trace elements, oxygen, chromium and titanium isotopes, and mid-IR spectroscopy. *Geochim. Cosmochim. Acta* **203**, 381–403 (2017).
162. M. E. Sanborn, Q.-Z. Yin, Chromium isotopic composition of the anomalous eucrites: An additional geochemical parameter for evaluating their origin. *Lunar Planet Sci. Conf. XLV*, 2018 (2014).
163. J. Gattacceca, B. P. Weiss, M. Gounelle, New constraints on the magnetic history of the CV parent body and the solar nebula from the Kaba meteorite. *Earth Planet. Sci. Lett.* **455**, 166–175 (2016).
164. H. Wang, B. P. Weiss, X.-N. Bai, B. G. Downey, J. Wang, J. Wang, C. Suavet, R. R. Fu, M. E. Zucolotto, Lifetime of the solar nebula constrained by meteorite paleomagnetism. *Science* **355**, 623–627 (2017).
165. P. H. Warren, Stable isotopes and the noncarbonaceous derivation of ureilites, in common with nearly all differentiated planetary materials. *Geochim. Cosmochim. Acta* **75**, 6912–6926 (2011).
166. A. Scheinberg, R. R. Fu, L. T. Elkins-Tanton, B. P. Weiss, Asteroid differentiation: Melting and large-scale structure, in *Asteroids IV*, P. Michel, F. DeMeo, W. F. Bottke, Eds. (University of Arizona Press, 2015), pp. 533–552.
167. D. Herčik, H.-U. Auster, D. Constantinescu, J. Blum, K.-H. Fornaçon, M. Fujimoto, K. Gebauer, J.-T. Grundmann, C. Güttler, O. Hillenmaier, T.-M. Ho, A. Hördt, C. Krause, E. Kührt, L. Lorda, A. Matsuoka, U. Motschmann, A. Moussi-Soffys, I. Richter, K. Sasaki, F. Scholten, B. Stoll, B. P. Weiss, F. Wolff, K.-H. Glassmeier, Magnetic properties of asteroid (162173) Ryugu. *J. Geophys. Res.* **125**, e2019JE006035 (2020).
168. P. Heinisch, H.-U. Auster, I. Richter, K. H. Glassmeier, Revisiting the magnetization of comet 67P/Churyumov-Gerasimenko. *Astron. Astrophys.* **630**, A46 (2019).
169. I. Richter, H. U. Auster, K. H. Glassmeier, C. Koenders, C. M. Carr, U. Motschmann, J. Müller, S. McKenna-Lawlor, Magnetic field measurements during the ROSETTA flyby at asteroid (21)Lutetia. *Planet. Space Sci.* **66**, 155–164 (2012).
170. H. Sawada, R. Okazaki, S. Tachibana, K. Sakamoto, Y. Takano, C. Okamoto, H. Yano, Y. Miura, M. Abe, S. Hasegawa, T. Noguchi; Hayabusa2 SMP Team, Hayabusa2 sampler: Collection of asteroidal surface material. *Space Sci. Rev.* **208**, 81–106 (2017).
171. J. B. Biersteker, B. P. Weiss, P. Heinisch, D. Herčik, K.-H. Glassmeier, H.-U. Auster, Implications of *Philae* magnetometry measurements at comet 67P/Churyumov–Gerasimenko for the nebular field of the outer solar system. *Astrophys. J.* **875**, 39 (2019).
172. J. Blum, B. Gundlach, M. Krause, M. Fulle, A. Johansen, J. Agarwal, I. von Borstel, X. Shi, X. Hu, M. S. Bentley, F. Capaccioni, L. Colangeli, V. D. Corte, N. Fougere, S. F. Green, S. Ivanovski, T. Mannel, S. Merouane, A. Migliorini, A. Rotundi, R. Schmied, C. Snodgrass, Evidence for the formation of comet 67P/Churyumov-Gerasimenko through gravitational collapse of a bound clump of pebbles. *Mon. Not. R. Astr. Soc.* **469**, S755–S773 (2017).
173. O. J. Stenzel, M. Hilchenbach, S. Merouane, J. Paquette, K. Varmuza, C. Engrand, F. Brandstätter, C. Koeberl, L. Ferrière, P. Filzmoser, S. Siljeström; COSIMA team, Similarities in element content between comet 67P/Churyumov–Gerasimenko coma dust and selected meteorite samples. *Mon. Not. R. Astr. Soc.* **469**, S492–S505 (2017).
174. D. Brownlee, D. Joswiak, G. Matrajt, Overview of the rocky component of Wild 2 comet samples: Insight into the early solar system, relationship with meteoritic materials and the differences between comets and asteroids. *Meteorit. Planet. Sci.* **47**, 453–470 (2012).
175. A. Sicilia-Aguilar, L. W. Hartmann, J. Hernández, C. Briceño, N. Calvet, Cepheus OB2: Disk evolution and accretion at 3-10 Myr. *Astrophys. J.* **130**, 188–209 (2005).
176. D. L. Schrader, R. R. Fu, S. J. Desch, J. Davidson, The background temperature of the protoplanetary disk within the first four million years of the Solar System. *Earth Planet. Sci. Lett.* **504**, 30–37 (2018).
177. R. R. Fu, B. P. Weiss, D. L. Schrader, B. C. Johnson, in *Chondrules: Records of Protoplanetary Disk Processes*, A. N. Krot, E. R. D. Scott, B. Reipurth, Eds. (Cambridge Univ. Press, 2018), pp. 324–340.
178. R. Oran, B. P. Weiss, O. Cohen, Were chondrites magnetized by the early solar wind? *Earth Planet. Sci. Lett.* **492**, 222–231 (2018).
179. C. Espaillat, J. Muzerolle, J. Najita, S. Andrews, Z. Zhu, N. Calvet, S. Kraus, J. Hashimoto, A. Kraus, P. D'Alessio, An Observational Perspective of Transitional Disks, in *Protostars and Planets VI*, H. Beuther, R. S. Klessen, C. P. Dullemond, T. Henning, Eds. (University of Arizona Press, 2014), pp. 497–520.
180. B. Ercolano, I. Pascucci, The dispersal of planet-forming discs: Theory confronts observations. *R. Soc. Open Sci.* **4**, 170114 (2017).
181. J. E. Owen, The origin and evolution of transition discs: Successes, problems, and open questions. *Publ. Astron. Soc. Australia* **33**, e005 (2016).
182. B. C. Johnson, K. J. Walsh, D. A. Minton, A. N. Krot, H. F. Levison, Timing of the formation and migration of giant planets as constrained by CB chondrites. *Sci. Adv.* **2**, e1601658 (2016).
183. D. L. Schrader, K. Nagashima, S. R. Waitukaitis, J. Davidson, T. J. McCoy, H. C. Connolly Jr., D. S. Lauretta, The retention of dust in protoplanetary disks: Evidence from agglomeratic olivine chondrules from the outer Solar System. *Geochim. Cosmochim. Acta* **223**, 405–421 (2018).
184. R. Helled, P. Bodenheimer, M. Podolak, A. Boley, F. Meru, S. Nayakshin, J. J. Fortney, L. Mayer, Y. Alibert, A. P. Boss, Giant Planet Formation, Evolution, and Internal Structure, in *Protostars and Planets VI*, H. Beuther, C. P. Dullemond, R. S. Klessen, T. K. Henning, Eds. (University of Arizona Press, 2014), pp. 643–666.
185. A. Johansen, M. Lambrechts, Forming planets via pebble accretion. *Annu. Rev. Earth Planet. Sci.* **45**, 359–387 (2017).
186. J. J. Lissauer, O. Hubickyj, G. D'Angelo, P. Bodenheimer, Models of Jupiter's growth incorporating thermal and hydrodynamic constraints. *Icarus* **199**, 338–350 (2009).

187. O. Gressel, J. P. Ramsey, C. Brinch, R. P. Nelson, N. J. Turner, S. Bruderer, Global hydromagnetic simulations of protoplanetary disks with stellar irradiation and simplified thermochemistry. *Astrophys. J.* **896**, 126 (2020).
188. L. Wang, X.-N. Bai, J. Goodman, Global simulations of protoplanetary disk outflows with coupled non-ideal magnetohydrodynamics and consistent thermochemistry. *Astrophys. J.* **874**, 90 (2019).
189. X.-N. Bai, J. M. Stone, Hall effect–mediated magnetic flux transport in protoplanetary disks. *Astrophys. J.* **836**, 46 (2017).
190. J. A. Wood, Formation of chondritic refractory inclusions: The astrophysical setting. *Geochim. Cosmochim. Acta* **68**, 4007–4021 (2004).
191. N. T. Kita, T. Ushikubo, Evolution of protoplanetary disk inferred from ^{26}Al chronology of individual chondrules. *Meteorit. Planet. Sci.* **47**, 1108–1119 (2012).
192. O. Pravdivtseva, A. Meshik, C. M. Hohenberg, The I-Xe record: Early onset of aqueous alteration in magnetites separated from CM and CV chondrites. *Lunar Planet Sci. Conf. XLIV* , 3104 (2013).
193. W. Fujiya, N. Sugiura, H. Hotta, K. Ichimura, Y. Sano, Evidence for the late formation of hydrous asteroids from young meteoritic carbonates. *Nat. Commun.* **3**, 627 (2012).
194. P. Koefoed, Y. Amelin, Q.-Z. Yin, J. Wimpenny, M. E. Sanborn, T. Iizuka, A. J. Irving, U–Pb and Al–Mg systematics of the ungrouped achondrite Northwest Africa 7325. *Geochim. Cosmochim. Acta* **183**, 31–45 (2016).
195. F. L. H. Tissot, N. Dauphas, T. L. Grove, Distinct ^{238}U/^{235}U ratios and REE patterns in plutonic and volcanic angrites: Geochronologic implications and evidence for U isotope fractionation during magmatic processes. *Geochim. Cosmochim. Acta* **213**, 593–617 (2017).
196. Y. Amelin, U-Pb ages of angrites. *Geochim. Cosmochim. Acta* **72**, 221–232 (2008).
197. L. Spivak-Birndorf, M. Wadhwa, P. Janney, ^{26}Al–^{26}Mg systematics in D'Orbigny and Sahara 99555 angrites: Implications for high-resolution chronology using extinct chronometers. *Geochim. Cosmochim. Acta* **73**, 5202–5211 (2009).
198. M. Schiller, J. N. Connelly, A. C. Glad, T. Mikouchi, M. Bizzarro, Early accretion of protoplanets inferred from a reduced inner solar system ^{26}Al inventory. *Earth Planet. Sci. Lett.* **420**, 45–54 (2015).
199. Y. Amelin, The U-Pb systematics of angrite Sahara 99555. *Geochim. Cosmochim. Acta* **72**, 4874–4885 (2008).
200. R. E. Zartman, E. Jagoutz, S. A. Bowring, Pb-Pb dating of the D'Orbigny and Asuka 881371 angrites and a second absolute time calibration of the Mn-Cr chronometer. *Lunar Planet. Sci.* **38**, 1580 (2006).
201. J. Bollard, J. N. Connelly, M. J. Whitehouse, E. A. Pringle, L. Bonal, J. K. Jørgensen, Å. Nordlund, F. Moynier, M. Bizzarro, Early formation of planetary building blocks inferred from Pb isotopic ages of chondrules. *Sci. Adv.* **3**, e1700407 (2017).
202. G. Budde, T. S. Kruijer, T. Klein, Hf-W chronology of CR chondrites: Implications for the timescales of chondrule formation and the distribution of ^{26}Al in the solar nebula. *Geochim. Cosmochim. Acta* **222**, 284–304 (2018).
203. D. L. Schrader, K. Nagashima, A. N. Krot, R. C. Ogliore, Q.-Z. Yin, Y. Amelin, C. H. Stirling, A. Kaltenbach, Distribution of ^{26}Al in the CR chondrite chondrule-forming region of the protoplanetary disk. *Geochim. Cosmochim. Acta* **201**, 275–302 (2017).
204. X. Hua, G. R. Huss, S. Tachibana, T. G. Sharp, Oxygen, silicon, and Mn-Cr isotopes of fayalite in the Kaba oxidized CV3 chondrite: Constraints for its formation history. *Geochim. Cosmochim. Acta* **69**, 1333–1348 (2005).
205. T. L. Norris, A. J. Gancarz, D. J. Rokop, K. W. Thomas, Half-life of ^{26}Al. *J. Geophys. Res.* **88**, B331–B333 (1983).
206. B. Jacobsen, Q.-z. Yin, F. Moynier, Y. Amelin, A. N. Krot, K. Nagashima, I. D. Hutcheon, H. Palme, ^{26}Al–^{26}Mg and ^{207}Pb–^{206}Pb systematics of Allende CAIs: Canonical solar initial ^{26}Al/^{27}Al ratio reinstated. *Earth Planet. Sci. Lett.* **272**, 353–364 (2008).
207. O. Pravdivtseva, A. Meshik, C. M. Hohenberg, A. N. Krot, I–Xe systematics of the impact plume produced chondrules from the CB carbonaceous chondrites: Implications for the half-life value of ^{129}I and absolute age normalization of ^{129}I–^{129}Xe chronometer. *Geochim. Cosmochim. Acta* **201**, 320–330 (2017).
208. J. D. Gilmour, S. A. Crowther, The I-Xe chronometer and its constraints on the accretion and evolution of planetesimals. *Geochem. J.* **51**, 69–80 (2017).
209. D. P. Glavin, A. Kubny, E. Jagoutz, G. W. Lugmair, Mn-Cr isotope systematics of the D'Orbigny angrite. *Geochim. Cosmochim. Acta* **39**, 693–700 (2004).
210. Y. Amelin, A. Kaltenbach, T. Iizuka, C. H. Stirling, T. R. Ireland, M. Petaev, S. B. Jacobsen, U–Pb chronology of the Solar System's oldest solids with variable ^{238}U/^{235}U. *Earth Planet. Sci. Lett.* **300**, 343–350 (2010).
211. G. J. Taylor, P. Maggiore, E. Scott, A. Rubin, K. Keil, Original structures, and fragmentation and reassembly histories of asteroids: Evidence from meteorites. *Icarus* **69**, 1–13 (1987).
212. A. H. Jaffey, K. F. Flynn, L. E. Glendenin, W. C. Bentley, A. M. Essling, Precision measurement of half-lives and specific activities of ^{235}U and ^{238}U. *Phys. Rev. C* **4**, 1889–1906 (1971).
213. A. Goldmann, G. A. Brennecka, J. Noordman, S. Weyer, M. Wadhwa, The uranium isotopic composition of the Earth and the Solar System. *Geochim. Cosmochim. Acta* **148**, 145–158 (2015).
214. R. J. Reisener, J. I. Goldstein, Ordinary chondrite metallography: Part 1. Fe-Ni taenite cooling experiments. *Meteorit. Planet. Sci.* **38**, 1669–1678 (2003).

Acknowledgments: We thank D. J. Stevenson and an anonymous reviewer for thoughtful reviews and M. E. Brown for editing the paper. We also thank P. Armitage, J. Biersteker, J. F. J. Bryson, L. I. Cleeves, T. Bosak, S. Desch, A. Johansen, N. Kita, T. Kleine, O. Pravdivtseva, S. T. Stewart, F. Tissot, and J. Wisdom for helpful discussions. **Funding:** B.P.W. thanks Thomas F. Peterson Jr. for support. X.-N.B. acknowledges support from the Youth Thousand Talents Program. **Author contributions:** B.P.W. and X.-N.B. contributed to all sections of the paper, with B.P.W. organizing the overall manuscript and leading the sections on meteorite and asteroid magnetism and X.-N.B. leading the sections on theory and astronomical observations. R.R.F. led the section on chondrule formation and contributed to the section on meteorite observations. **Competing interests:** The authors declare that they have no competing interests. **Data and materials availability:** All data are available in the published literature. Key dates and paleomagnetic constraints are compiled in tables S1 and S2.

Submitted 17 December 2019
Accepted 10 November 2020
Published 1 January 2021
10.1126/sciadv.aba5967

Citation: B. P. Weiss, X.-N. Bai, R. R. Fu, History of the solar nebula from meteorite paleomagnetism. *Sci. Adv.* **7**, eaba5967 (2021).

Science Advances

History of the solar nebula from meteorite paleomagnetism

Benjamin P. Weiss, Xue-Ning Bai and Roger R. Fu

Sci Adv **7** (1), eaba5967.
DOI: 10.1126/sciadv.aba5967

Science Advances
AAAS

advances.sciencemag.org/cgi/content/full/7/1/eaba5967/DC1

Supplementary Materials for

History of the solar nebula from meteorite paleomagnetism

Benjamin P. Weiss*, Xue-Ning Bai*, Roger R. Fu

*Corresponding author. Email: bpweiss@mit.edu (B.P.W.); xbai@tsinghua.edu.cn (X.-N.B.)

Published 1 January 2021, *Sci. Adv.* **7**, eaba5967 (2021)
DOI: 10.1126/sciadv.aba5967

This PDF file includes:

Supplementary Text
Tables S1 and S2

Supplementary Text

Equations in Système International (SI) units

The equations in the main text are given in cgs units, which are in common usage in the astronomical community. Given that the geoscience and paleomagnetism communities typically use SI units (mks), here we list the equations in the latter units:

$$\frac{\partial(2\pi R\Sigma j)}{\partial t}+\frac{\partial\left(\dot{M}_{\mathrm{acc}}j\right)}{\partial R}+\frac{\partial}{\partial R}\left[2\pi R^2\int_{z_{\mathrm{bot}}}^{z_{\mathrm{top}}}dz\left(\overline{\rho\delta v_R\delta v_\phi}-\frac{\overline{B_R B_\phi}}{\mu_0}\right)\right]$$
$$+2\pi R^2\left(\overline{\rho v_z v_\phi}-\frac{\overline{B_z B_\phi}}{\mu_0}\right)\Bigg|_{z_{\mathrm{bot}}}^{z_{\mathrm{top}}}=0 \tag{1}$$

$$B_{\mathrm{mid},R\phi}\cong 72\mu\,\mathrm{T}\left(\frac{M}{M_\odot}\right)^{1/4}\left(\frac{\dot{M}_{\mathrm{acc}}}{10^{-8}M_\odot\mathrm{y}^{-1}}\right)^{1/2}\left(\frac{fH}{L_z}\right)^{1/2}\left(\frac{R}{\mathrm{AU}}\right)^{-11/8} \tag{2}$$

$$B_{\mathrm{mid},z\phi}=mB_{\mathrm{base},z\phi}\cong m\,(6.5\mu\mathrm{T})\left(\frac{M}{M_\odot}\right)^{1/4}\left(\frac{\dot{M}_{\mathrm{acc}}}{10^{-8}M_\odot\mathrm{y}^{-1}}\right)^{1/2}f'^{\,1/2}\left(\frac{R}{\mathrm{AU}}\right)^{-5/4} \tag{3}$$

$$\boldsymbol{F}=\boldsymbol{J}\times\boldsymbol{B}=\frac{(\nabla\times\boldsymbol{B})\times\boldsymbol{B}}{\mu_0}=\boldsymbol{\kappa}\frac{B^2}{\mu_0}-\nabla_\perp\frac{B^2}{2\mu_0}=\boldsymbol{F_T}+\boldsymbol{F_P} \tag{4}$$

$$\frac{\partial\boldsymbol{B}}{\partial t}=\nabla\times(\boldsymbol{v}\times\boldsymbol{B})-\mu_0\nabla\times(\eta_O\boldsymbol{J}+\eta_H\boldsymbol{J}\times\boldsymbol{b}+\eta_A\boldsymbol{J}_\perp) \tag{5}$$

Table S1. Radiometric age constraints on meteorite records of nebular magnetism.

A. Meteorites that record a nebular magnetic field

Group	Meteorites	Lithology	Technique	Age (Ma After Standard/Ago)	Uncert. (Ma)[1]	Standard	Age (Ma After CAIs)[2]	Uncert. (Ma)	Ref.
LL	Semarkona	chondrule	Al-Mg[3,4]	2.03 0.75	0.81 0.81	CAIs	2.03 0.63	0.81 0.81	(*191*)
LL NRM age[3]							2.03 (0.75)	0.81 (0.81)	
CM	Murchison	magnetite	I-Xe[5]	-1.7	0.2	Shallowater	2.90	0.39	(*192*)
	Murchison	carbonate	Mn-Cr[6]	1.20	1.57	D'Orbigny	4.99	1.59	(*193*)
CM	Y-791198	carbonate	Mn-Cr[6]	-0.11	1.11	D'Orbigny	3.68	1.14	(*193*)
CM	ALH 83100	carbonate	Mn-Cr[6]	0.95	0.79	D'Orbigny	4.75	0.83	(*193*)
CM	Samaya	carbonate	Mn-Cr[6]	-0.07	0.49	D'Orbigny	3.73	0.55	(*193*)
CM NRM age[7]							2.90 (3.54) (4.03) (4.66)	0.39 (0.42) (0.45) (0.47)	
Inferred minimum lifetime of nebular field in noncarbonaceous reservoir[8]							*>1.22*		
Inferred minimum lifetime of nebular field in carbonaceous reservoir[8]							*>2.51*		

B. Meteorites that record null to weak magnetic field conditions.

Group	Meteorites	Lithology	Technique	Age (Ma After Standard/Ago)	Uncert. (Ma)[1]	Standard	Age (Ma After CAIs)[2]	Uncert. (Ma)	Ref.
Ungrouped	NWA 7325	bulk	Al-Mg[4]	5.24 3.97	0.05 0.05	CAIs	5.24 3.97	0.05 0.05	(*194*)
		bulk	U-Pb[9, 10]	4563.4	2.6	-	3.90	2.60	(*194*)
NWA 7325 null magnetization age[11]							5.24 (3.97) (3.90) (4.54)	0.05 (0.05) (2.60) (2.61)	
Angrite	D'Orbigny	bulk	U-Pb[9, 12]	4563.51	0.18	-	3.79	0.24	(*195, 196*)
Angrite	D'Orbigny	bulk	Al-Mg[4, 13]	4.72 4.96	0.19 0.04	CAIs	4.72 4.96	0.19 0.04	(*197*) (*198*)
Angrite	Sahara 99555	bulk	U-Pb[9, 14]	4564.07	0.43	-	3.23	0.46	(*195, 199*)
Angrite	Sahara 99555	bulk	Al-Mg[4, 13]	4.70 5.05	0.40 0.05	CAIs	4.70 5.05	0.40 0.05	(*197*) (*198*)
Angrite	A-881371	bulk	U-Pb[9]	4562.4	1.6	-	4.90	1.61	(*200*)
Angrite null magnetization age[15]							3.71 (4.35) (4.71) (5.00)	0.23 (0.27) (0.17) (0.03)	
CR	GRA 95229 LAP 02342	chondrule	U-Pb[9, 16]	4563.24-4567.26		-	0.04-4.06	-	(*201*)
		chondrule	Hf-W[17]	3.62	0.28	CAIs	3.62	0.28	(*202*)
		chondrule	Al-Mg[4, 18]	3.68 2.41	0.22 0.22	CAIs	3.68 2.41	0.22 0.22	(*203*)
CR weak-field magnetization age[19]							3.68 (2.41) (4.06) (0.04)	0.22 (0.22) (0.66) (0.43)	
CV	Kaba	magnetite	I-Xe[5]	-0.1	1.2	Shallowater	4.50	1.25	(*192*)
	Kaba	fayalite	Mn-Cr[6]	2.39	0.44	D'Orbigny	6.19	0.50	(*204*)
	A-881317	fayalite	Mn-Cr[6]	0.29	0.77	D'Orbigny	4.08	0.81	(*148*)

CV null magnetization age[20]	4.08 (4.72) (4.50) (5.14)	0.81 (0.82) (1.25) (1.25)
Inferred maximum lifetime of nebular field in noncarbonaceous reservoir[21]	*<3.94*	
Inferred maximum lifetime of nebular field in carbonaceous reservoir[21]	*<4.89*	

Notes: The first column gives the meteorite group name, the second column gives the meteorite name, the third column lists the lithology dated, the fourth column lists the chronometer, the fifth column lists the absolute age for U-Pb analyses or relative age after the standard for the relative chronometers (positive values = younger than standard), the sixth column lists the 2-standard deviation uncertainty in millions of years (Ma) (for simplicity, uncertainties are reported as the mean of the upper and lower age uncertainties), the seventh column lists the age of the standard for relative chronometers, the eighth column lists the age after the formation relative to calcium aluminum inclusions (CAIs), the ninth column lists the 2-standard deviation uncertainty for the age relative to CAIs, and the tenth column lists the references.

[1]Does not take into account uncertainties associated with the isotopic composition of the age standards or uncertainties associated with decay constants.

[2]Incorporates uncertainty on CAI age for measurements that do not use CAIs as a direct standard as specified in column 7 (i.e., for all dates except those from the Al-Mg system).

[3]Mean value and standard deviation of ages of 25 type I and II chondrules (*191*). Detailed dataset provided by personal communication from N. Kita (2018).

[4]Al-Mg ages are calculated using a decay constant of 9.83×10^{-7} y^{-1} (*205*). The top age is calculated assuming that CAIs have a canonical initial $^{26}Al/^{27}Al$ composition of 5.23×10^{-5} (*206*) and that this was uniform throughout the inner solar system. The bottom age is calculated instead assuming a nonuniform initial $^{26}Al/^{27}Al$ composition with a value of 1.33×10^{-5} in the formation region of the meteorite (*198, 201*).

[5]I-Xe ages are calculated using a decay constant of 4.41×10^{-8} y^{-1} and are referenced to the Shallowater meteorite standard, which is taken to have an absolute age of 4562.7 ± 0.3 Ma (*207, 208*).

[6]Mn-Cr ages are calculated using a decay constant of 1.87×10^{-7} y^{-1} and are referenced to the D'Orbigny meteorite standard, which is taken to have an absolute age of 4563.51 ± 0.18 Ma (*195, 196*) and an initial $^{53}Mn/^{55}Mn$ composition of $(3.24 \pm 0.04)\times10^{-6}$ (*209*).

[7]Top row is the I-Xe magnetite age referenced to the nominal weighted mean U-Pb CAI age of 4567.30 ± 0.16 Ma from refs. (*142, 210*); this is our preferred age since it directly dates the formation of the main magnetization carriers and is referenced to a CAI age in the refereed literature. Ages in parentheses at bottom are alternative dates calculated as follows. The second age is calculated using the same I-Xe magnetite age but referenced to an alternative U-Pb CAI age of 4567.94 ± 0.21 Ma (*143*). The third age is from Mn-Cr carbonate ages, calculated by weighting the means with the inverse of the square of the standard deviation (*211*) and referenced to the nominal U-Pb CAI age (*142, 210*). The fourth age is calculated using the same mean Mn-Cr age but referenced to the alternative U-Pb CAI age (*143*).

[8]The minimum nebular field lifetimes in the noncarbonaceous and carbonaceous reservoirs are inferred from the two most stringent constraints in these reservoirs: the LL and CM chondrites, respectively. The lifetimes are calculated as the mean relative ages of each relative to the nominal CAI formation ages minus their 2-standard deviation uncertainties as listed earlier in table.

[9]U-Pb ages are calculated using ^{235}U and ^{238}U decay constants of 9.84×10^{-10} y^{-1} and 1.55×10^{-10} y^{-1}, respectively (*212*).

[10]Because $^{238}U/^{235}U$ was not measured for NWA 7325, we assume a value of 137.794 ± 0.027, the currently estimated bulk solar system value (*213*).

[11]Top row is the Al-Mg age using the canonical initial $^{26}Al/^{27}Al$ ratio (*206*); this is our preferred age because it has lower uncertainties relative to the U-Pb dates due to the higher precision of the measurements and because the Al-Mg standard is CAIs (such that the absolute ages of CAIs do not contribute to the uncertainty). Ages in parentheses at bottom are alternative dates calculated as follows. The second age is the Al-Mg age using the alternative initial $^{26}Al/^{27}Al$ ratio of refs. (*198, 201*). The third age is the U-Pb age referenced to the nominal U-Pb CAI age (*142, 210*). The fourth age is the same U-Pb age but referenced to the alternative U-Pb CAI age (*143*).

[12]Using the measured $^{238}U/^{235}U$ for D'Orbigny of 137.793 ± 0.025 (*195*).

[13]Top and bottoms rows are the Al-Mg age using the angrite's initial $^{26}Al/^{27}Al$ ratio as measured by refs. (*197*) and (*198*), respectively. Both ages are calculated assuming the canonical CAI initial $^{26}Al/^{27}Al$ ratio.

[14]Using the measured $^{238}U/^{235}U$ for Sahara 99555 of 137.805 ± 0.029 (*195*).

[15]Top row is calculated using the mean U-Pb age of D'Orbigny and Sahara 99555 weighted by the inverse of the square of their standard deviations (*211*) referenced to the weighted mean U-Pb CAI age of 4567.30 ± 0.16 Ma from refs (*142, 210*); this is our preferred age because it is an absolute age and is referenced to a CAI age in the refereed literature. The ages in parentheses at bottom are alternative dates calculated as follows. The second age is the mean U-Pb age referenced to the alternative U-Pb CAI age (*143*). The third age is the uncertainty-weighted mean Al-Mg age for D'Orbigny and Sahara 99555 using the data of ref. (*197*) assuming the canonical CAI initial $^{26}Al/^{27}Al$ ratio. The fourth age is the uncertainty-weighted mean Al-Mg age for D'Orbigny and Sahara 99555 using the data of ref. (*198*) again assuming the canonical CAI initial $^{26}Al/^{27}Al$ ratio.

[16]The full range of measured U-Pb ages from chondrules from the CR chondrites from NWA 6043 and NWA 7655.

[17]Using Hf-W ages from chondrules from 4 other CR chondrites.

[18]Mean value and standard deviation of ages of 21 chondrules from ref. (*203*)'s groups B and C including chondrules from GRA 95209.

[19]Top row is the Al-Mg age using the canonical initial $^{26}Al/^{27}Al$ ratio (*206*); this is our preferred age because it has lower uncertainties relative to the U-Pb dates due to the higher precision of the measurements and because the Al-Mg standard is CAIs (such that the absolute ages of CAIs do not contribute to the uncertainty). Ages in parentheses at bottom are alternative dates calculated as follows. The second age is the Al-Mg age using the alternative initial $^{26}Al/^{27}Al$ ratio of refs. (*198, 201*). The third age is the youngest U-Pb chondrule age referenced to the nominal U-Pb CAI age (*142, 210*). The fourth age is the same oldest U-Pb chondrule age referenced to the same nominal U-Pb CAI age.

[20]The first age is the Mn-Cr fayalite age referenced to the nominal U-Pb CAI age (*142, 210*); this is our preferred age because it was based on a fayalite standard with similar composition as the natural material being dated and is referenced to a CAI age in the refereed literature. Ages in parentheses at bottom are alternative ages as follows. The second age is calculated using the same Mn-Cr age but referenced to the alternative U-Pb CAI age of 4567.94 ± 0.21 Ma (*143*). The third age is the I-Xe magnetite age referenced to the nominal U-Pb CAI age (*142, 210*). Although the I-Xe dates have the advantage over Mn-Cr ages in directly dating the formation of magnetite, this age is not yet reported in a refereed publication. The fourth age is the same I-Xe age but referenced to the alternative U-Pb CAI age (*143*).

[21]The maximum nebular field lifetimes in the noncarbonaceous and carbonaceous reservoirs are inferred from the two most stringent constraints in these reservoirs: the volcanic angrites and the CV chondrite Kaba, respectively. The lifetimes are calculated as the mean relative ages of each relative to the nominal CAI formation ages plus their 2-standard deviation uncertainties as listed earlier in table.

Table S2. Paleointensity constraints on the solar nebula magnetic field from meteorites.

A. Meteorites that record a nebular magnetic field

Meteorite	Group	Reservoir	Lithology	Distance (AU)	NRM	Method	Timescale	Field (G)	Ref.
Semarkona	LL	NC	chondrules	2.20	TRM	ARM[1]	~1-10^3 h	0.54 ± 0.21	(*10*)
Adopted LL chondrite paleointensity				2 ± 1				0.54 ± 0.21	
Cold Bokkeveld	CM	C	bulk	3.76	CRM	IRM[2]	>1 to 10^6 y	>0.03	(*134*)
Mighei	CM	C	bulk	3.76	CRM	IRM[3]	>1 to 10^6 y	>0.02	(*134*)
Murchison	CM	C	bulk	3.76	CRM	IRM[3]	>1 to 10^6 y	>0.02	(*134*)
Murray	CM	C	bulk	3.76	CRM	IRM[3]	>1 to 10^6 y	>0.04	(*134*)
Nogoya	CM	C	bulk	3.76	CRM	IRM[3]	>1 to 10^6 y	>0.02	(*134*)
Paris	CM	C	bulk	3.76	CRM	IRM[4]	>1 to 10^6 y	>0.06	(*134*)
Adopted CM chondrite paleointensity				5 ± 2				>0.06	

B. Meteorites that record null or weak magnetic field conditions.

NWA 7325	Ungrouped	NC	bulk	2 ± 1[5]	TRM	ARM, IRM, TRM[6]	<10 h[7]	<0.034	(*124*)
Adopted NWA 7325 paleointensity				2 ± 1				<0.034	
D'Orbigny	angrite	NC	bulk	2 ± 1[5]	TRM	ARM, IRM, TRM[8]	10-100 h	<0.006	(*164*)
Sahara 99555	angrite	NC	bulk	2 ± 1[5]	TRM	ARM, IRM, TRM[9]	10-100 h	<0.006	(*164*)
A-881371	angrite	NC	bulk	2 ± 1[5]	TRM	ARM, IRM[10]	10-100 h	<0.004	(*164*)
Adopted angrite paleointensity				2 ± 1				<0.006	
GRA 95229	CR	C	chondrules	3.84	TRM	ARM	~1-10^3 h	<0.16	(*160*)
LAP 02342	CR	C	chondrules	3.84	TRM	ARM	~1-10^3 h	<0.08	(*160*)
Adopted CR chondrite paleointensity				5 ± 2				<0.08	
Kaba	CV	C	bulk	3.60	CRM	TRM[11]	>1 to 10^6 y	<0.003	(*163*)
Adopted CV chondrite paleointensity				5 ± 2				<0.003	

Notes: The first column gives the meteorite name, the second column gives the meteorite group, the third column lists the nebular isotopic reservoir from which the meteorite was derived (NC = noncarbonaceous; C = carbonaceous) (*161, 165*), the fourth column lists the type of lithology analyzed, the fifth column lists the formation distance, the sixth column lists the form of natural remanent magnetization (NRM) analyzed (TRM = thermoremanent magnetization; CRM = crystallization remanent magnetization), the seventh column lists the normalizing remanence used for the paleointensity experiments (ARM = anhysteretic remanent magnetization; IRM = isothermal remanent magnetization; TRM), the eighth column list the timescale of NRM acquisition (cooling from the Curie point to ambient temperatures for TRM or crystallization of the ferromagnetic minerals for CRM), the ninth column lists the paleointensity constraint, and the tenth column lists the references for the paleointensities. At the italicized row at the bottom of each meteorite group lists the distance and paleointensity constraints for each meteorite/meteorite group adopted by this study. The paleointensity values are corrected for the rotation of meteorite parent bodies, which is expected to reduce the recorded paleointensity relative to that of the nebula by a factor of 2 on average for non-tumbling rotation. In column 5, we report the formation locations for individual meteorites from ref. (*153*); however, for meteorite groups we instead more conservatively assume NC meteorites formed at 1-3 AU [i.e., within Jupiter's initial assumed formation location (*153*)], while C meteorites formed beyond Jupiter's assumed formation location but within 7 AU based on the H isotopic composition of their water contents (*153, 154*). These formation locations are overall highly uncertain.

[1]Mean paleointensity measured for 6 chondrules multiplied by 2 to account for non-processing rotation of the chondrules. Modeling of planetesimal nebular shocks demonstrates that chondrules formed by this process would cool through their Curie temperatures in a region where the magnetic field is close to that of the background unshocked nebula (*155*). Assuming this formation mechanism would remove the previous factor of 10 paleointensity uncertainty discussed by ref. (*10*).

[2]Using the ratio of residual NRM and residual IRM after demagnetization to 200 G. This paleointensity is likely a minimum value because it was estimated assuming the same efficiencies for CRM and TRM. Because we consider it likely that the paleofield recorded by CM chondrites is that of the nebula rather than that of their parent body, the

value listed here is twice that reported by ref. (*134*) to account for non-precessing rotation of the CM body relative to the nebular field [see ref. (*10*)].

[3]Using the REM' normalization technique (*122*) for the high coercivity (HC) range for single samples of each meteorite. This paleointensity is likely a minimum value because it was estimated assuming the same efficiencies for CRM and TRM. Because we consider it likely that the paleofield recorded by CM chondrites is that of the nebula rather than that of their parent body, the values listed here is twice that reported by ref. (*134*) to account for non-precessing rotation of the CM body relative to the nebular field [see ref. (*10*)].

[4]Mean value for 5 subsamples using the REM' normalization technique (*122*) for the HC range. This paleointensity is likely a minimum value because it was estimated assuming the same efficiencies for CRM and TRM. Because we consider it likely that the paleofield recorded by CM chondrites is that of the nebula rather than that of their parent body, the value listed here is twice that reported by ref. (*134*) to account for non-precessing rotation of the CM body relative to the nebular field [see ref. (*10*)].

[5]Ref. (*153*) does not report an estimate for the formation location for these meteorites. However, their Cr, O, and Ti isotopic compositions (*161, 165*) indicate they are part of the NC clan. Therefore, we estimate a formation location in the inner solar system (1-3 AU).

[6]Uncertainty-weighted mean value for HC/HT (high temperature) range from 6 experiments on subsamples B71 (ARM and IRM methods), B73 (ARM and IRM methods), B78 (TRM method) and B79 (TRM method) [see ref. (*124*) for details]. The value listed here is twice that reported by ref. (*134*) to account for non-precessing rotation of NWA 7325's parent body relative to the nebular field [see ref. (*10*)]. The estimated 2-standard deviation uncertainty on this upper limit is a factor of ~5 given uncertainties in the ratio of IRM to TRM [see ref. (*120*)].

[7]Upper limit based on the absence of kamacite exsolution from taenite, which occurs for cooling rates as fast as 0.13 °C s^{-1} (*214*). This constraint assumes kamacite nucleation in NWA 7325 was not otherwise inhibited by either the low-P content of the metal and absence of taenite-taenite grain boundaries.

[8]Grand mean for the HC/HT range computed from averaging the mean ARM paleointensity for 9 subsamples with the mean IRM paleointensity for 9 subsamples and multiplied by 2 to account for non-precessing rotation of the angrite parent body relative to the nebular field. The ARM and IRM means are computed as vector mean values [see ref. (*164*)]. The uncertainty on this upper limit is a factor of ~2 given uncertainties in the ratios of ARM and IRM to TRM (*164*).

[9]Grand mean for the HC/HT range computed from averaging the mean ARM paleointensity for 3 subsamples with the mean IRM paleointensity for 3 subsamples and multiplied by 2 to account for non-precessing rotation of the angrite parent body relative to the nebular field. The ARM and IRM means are computed as vector mean values [see ref. (*164*)]. The uncertainty on this upper limit is a factor of ~2 given uncertainties in the ratios of ARM and IRM to TRM (*164*).

[10]The mean paleointensity for the ARM and IRM for the HC range is -0.003 ± 0.005 G. Because a paleointensity cannot be less than zero, we add the uncertainty to the nominal value to yield an upper limit of 0.002 G. Multiplying this by a factor of 2 to account for non-precessing rotation of the angrite parent body relative to the nebular field gives the upper limit of 0.004 G stated in the table. The uncertainty on this upper limit is a factor of ~2 given uncertainties in the ratios of ARM and IRM to TRM (*164*).

[11]Mean upper limit measured for blocking temperatures >250°C for three subsamples and multiplied by 2 to account for non-precessing rotation of the CV body relative to ambient field environment [see ref. (*10*)]. This paleointensity assumes that the CRM in Kaba has an efficiency similar to that of TRM. This upper limit will rise if the CRM is less efficient than the TRM, making this paleointensity constraint particularly uncertain.